Final Report

Project Title: Combinatorial Platform for Discovery of Nanocrystal-Ink Based Earth Abundant Element PV with Efficiency Greater than 20%

Project Period: 10/01/11 – 1/31/16

Project Budget: $541,864

Submission Date: 4/29/16

Recipient: University of Washington

Address: 4333 Brooklyn Ave NE, 17th Floor
Seattle, WA 98195-9472

Award Number: DE-EE0005321

Project Team: Hugh W. Hillhouse (PI)

Contacts:
Hugh W. Hillhouse
Rehnberg Chair Professor of Chemical Engineering
Phone: (206) 685-5257
Fax: (206) 543-3778
Email: h2@uw.edu

Executive Summary:

Objectives: The project objectives formulated at the onset of the project (2011) effort were to: (1) Set-up and test a novel high-throughput ultrasonic spray coating thin film deposition platform for exploring the composition space of solution-processed kesterite solar cells. (2) Explore germanium alloying for tin in CZTSSe in order to be able to tune the bandgap and more importantly the conduction band edge. This could be used to create a back surface field to reflect minority carriers away from the back contact. (3) Use the high-throughput techniques developed to discover new extrinsic dopants to improve the performance of solution-processed CZTSSe-based thin film solar cells. In 2013, the project was expanded to include: (4) Development of photoluminescence techniques to accurate extract the quasi-Fermi level splitting from absolute intensity PL measurements.

Major Outcomes and Findings:

(1) We successfully developed an ultrasonic spray coating system that can be used to deposit thin chalcogenide films with composition gradients. 4 publications under the contract have been published with the instrument. The instrument was used to reveal the effects of intrinsic composition and examine the effects of 25 different dopant elements. Surprisingly, doping with most elements had little to no effect on the quasi-Fermi level splitting of bare films. A few elements were found to be detrimental including Fe, Co, and Ni. However, Li, Ge, and others were discovered to be beneficial. Ge and Li were explored in depth, and our best devices utilize lithium doping.

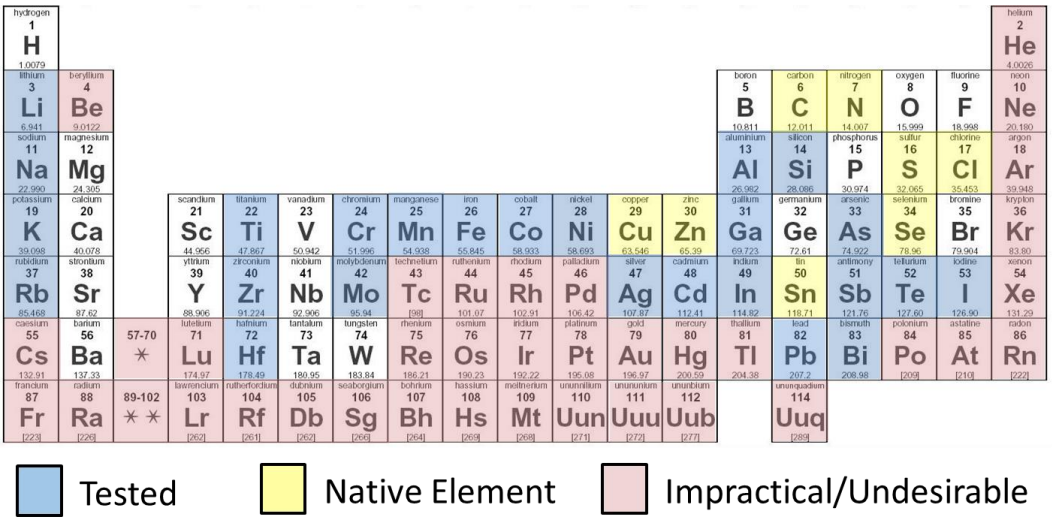

Figure 1. Summary of elements examined with the high-throughput experiments. Variations in the concentrations of native elemtents Cu, Zn, and Sn were examined. Small amounts of C, N, and Cl were present due to the molecular ink. In addition, 25 extrinsic dopants (indicated in blue) were tested for their effects on optoelectronic quality.

(2) We developed a new model of absorption coefficients, that when combined with absolute intensity photoluminescence, yield the steady-state quasi-Fermi level splitting and a way to quantify the sub-bandgap absorption. This has resulted in 2 publications on the method, with another in preparation. This is a significant development that should

impact other PV technologies. We have already received samples from 2 major PV companies to examine. Further, the model shows that tail states (potential fluctuations) in CZTSSe can only explain about 90 mV of loss in the open circuit voltage.

(3) We found that lithium doping has several beneficial effects on CZTSSe. It improves the open-circuit voltage, short circuit current, fill factor, and shunt resistance. By using scanning Kelvin probe microscopy (SKPM) and conductive AFM (along with device measurements, DLPC, and XPS), we discovered that lithium acts to increase the p-type doping in both the grain and grain boundaries (GBs). The effect is stronger in the GBs and changes the direction of the electric field at the GB. In lithium doped devices, an electric field repels minority carrier electrons away from the GB. This resulted in a publication and the fabrication of 11.8% efficient devices from a DMSO-thiourea molecular ink. The mechanism of action is most likely due to the formation of Li_{Cu}, which inhibits the formation of the donor defect Zn_{Cu}. This reduces compensation and increases the net p-type doping.

(4) By alloying with germanium, we have fabricated CZTGSSe devices with the best open-circuit voltage (relative the maximum theoretical open-circuit voltage for the bandgap) for any kesterite solar cell. The Voc/Voc,max is 63%, compared to 58% for the record efficiency cell from hydrazine. The origin of the increased voltage efficiency appears to be related to the conduction band off-set and the suppression of a deep defect (~0.8 eV), most likely due to Cu_{Sn}, but Sn_{Zn} or Sn_{Cu} are also possible.

All milestones and go/no-go metrics were met with exception of the device efficiency milestone (15% then 20%). However, under the contract, hydrazine-free CZTSSe device efficiencies increased from 7.2% at the start of the contract to 11.8% upon completion.

Impact, Perspective, and Path Forward: The tools developed with this contract (the combinatorial spray coater and photoluminescence analysis methods) are already having impact beyond CZTS. These methods are proving useful in discover effects in hybrid perovskites. The PL methods are particularly useful since they allow a fair assessment of the maximum possible open-circuit voltage without having to fabricate devices. With regard to kesterites, we believe that the effects of lithium doping are of significant importance. While we were able to achieve 11.8% from an DMSO/thiourea route, it is possible that record efficiency devices may be achieved with sputtering or hydrazine chemistry. However, clearly the most significant challenge to achieving high efficiency devices is overcoming the low voltages. The prevailing opinion (up to 2015) appears to be that Cu/Zn site disorder and the resulting potential fluctuations are the fundamental limitation. However, our experiments show that potential fluctuations only result in a 90 mV loss (in the radiative limit). Further, recent experiments with extended low temperature annealing that reduces Cu/Zn disorder have not shown high open-circuit voltages in high performance devices. Deep defects, particularly related to tin (Cu_{Sn}, Sn_{Zn} or Sn_{Cu}), may be the culprit. Our experiments with Ge alloying support this hypothesis. This points towards a path forward that may be used to increase the open circuit voltages even further.

Table of Contents

Section **Page Number**

1. Background 5

2. Introduction 6

3. Project Results and Discussion 8

    a. Task 1. Set-up of Liquid Delivery System for Ultrasonic Spray Coating 8
    b. Task 2. Variation of Stoichiometry in CZTSSe 10
    c. Task 3. Exploring Ge Substitution for Sn 21
    d. Task 4. Extrinsic Doping..... 26
    e. Task 5. Photoluminescence Characterization 30

4. Conclusions 35

5. Budget and Schedule 36

6. Path Forward 37

7. References 38

1. Background

In the development of both Cu(In,Ga)Se_2 (CIGS) and CdTe thin film solar cells, one of the most effective strategies for improving device efficiency has been to find extrinsic species that can dope the absorber layer and passivate intrinsic defects. $CdCl_2$ treatments of CdTe absorber layers enhance grain size,[1] passivate grain boundaries and surfaces,[2,3] and significantly improve the overall efficiency. For CIGS it has been shown repeatedly that sodium improves conductivity, open-circuit voltage, and fill factor.[4-6] Potassium surface treatments have also been shown to benefit CIGS by aiding in the formation of a buried homojunction and allowing for a thinner CdS layer.[7,8] Antimony and Bismuth have both been shown to aid in the crystallization of CIGS, leading to improved efficiency, particularly for devices processed at lower temperatures.[9-11]

Although these extrinsic species have been experimentally shown to benefit the absorbers, the exact mechanism is often still debated or unknown. For example, the benefits of sodium in CIGS were discovered when researchers substituted soda-lime glass for more traditional alkali-free substrates.[5] Soda-lime glass was used because it had a thermal expansion coefficient closer to that of CIGS, but it was quickly discovered that the anomalously high performance resulted from sodium diffusion into the absorber layer. Despite this realization, the exact role of Na in CIGS is still debated, and has been the subject of intense research over the last several decades. Several models have been proposed to explain the observed behavior including: the defect chemical model,[12] the positive electron acceptor model,[13,14] and the neutral hole barrier model.[15,16] These models differ in mechanism, but agree that Na helps passivate grain boundaries, improves conductivity, and reduces defect densities.

In recent years, concerns about the price and availability of the elements In and Te have spurred research into earth-abundant thin film materials. One of the leading candidates is $Cu_2ZnSn(S,Se)_4$ (CZTSSe), a material which bears many resemblances to CIGS in its structural and electronic properties, but is comprised of abundant, low-cost primary metals (metals mined for directly). At the onset of this research effort (2011) the record CZTSSe device yielded an efficiency of 9.7%.[17] A major drawback of the fabrication process was the use of large amounts of hydrazine, which is explosive, hepatotoxic,[18] and carcinogenic.[19] Alternatively, we had developed a nanocrystal-ink based approach that yielded devices with 7.2% efficiency[20-23] and a molecular ink approach that yielded 4.1% devices.

The focus of this research study (2011 to 2015) was develop tools (high-throughput deposition of many compositions and screening of optoelectronic quality) to rapidly explore the composition space of variations of the intrinsic elements (Cu, Zn, and Sn) and to discover other extrinsic elements that could be alloyed with CZTS or used to dope or passivate the material to achieve higher performance. Over the course of the research contract, we pioneered the DMSO-thiourea based molecular ink chemistry that has now yielded 11.8% efficient devices.[24,25] We were the first to reveal how the quasi-Fermi level splitting varies over the pseudo ternary composition space,[26] the first to show the dramatic effects that copper deficiency has on tin loss,[26] the first to discover the beneficial effects of lithium doping,[24] the first to test many new doping compositions (25 extrinsic elements explored), and reported a new sub-bandgap

absorption model that can be used along with absolute intensity photoluminescence to determine the quasi-Fermi level splitting of an absorber, even in the presence of sever band tails.[27]

Over the same period, CZTSSe devices reached 12.6% efficiency using hydrazine-based inks.[28] However, further efficiency improvements are needed to be competitive with current technologies. Comparing the performance of the world record CZTSSe device to the theoretical limits under AM1.5G illumination, it is clear that a low open-circuit voltage limits the power conversion efficiency. The world record CZTSSe device collects 81% of the maximum current (Jsc^{SQ}) but only produces 58% of the maximum voltage (Voc^{SQ}). Studies suggest that the low voltage results from a large quantity of intrinsic defects.[29,30] These defects are relatively shallow and are mostly compensated, but still lead to significant electrostatic potential fluctuations and reduced carrier mobility.[29-31]

2. Introduction

The broad approach of the project was to develop a method to deposit chalcogenide films with controlled lateral composition gradients (Task 1, Figure 2), develop methods to screen and characterize the gradients (Task 2 and 5), and to use both tools to explore the intrinsic composition space (Task 2), germanium alloying (Task 3), and extrinsic dopants (Task 4).

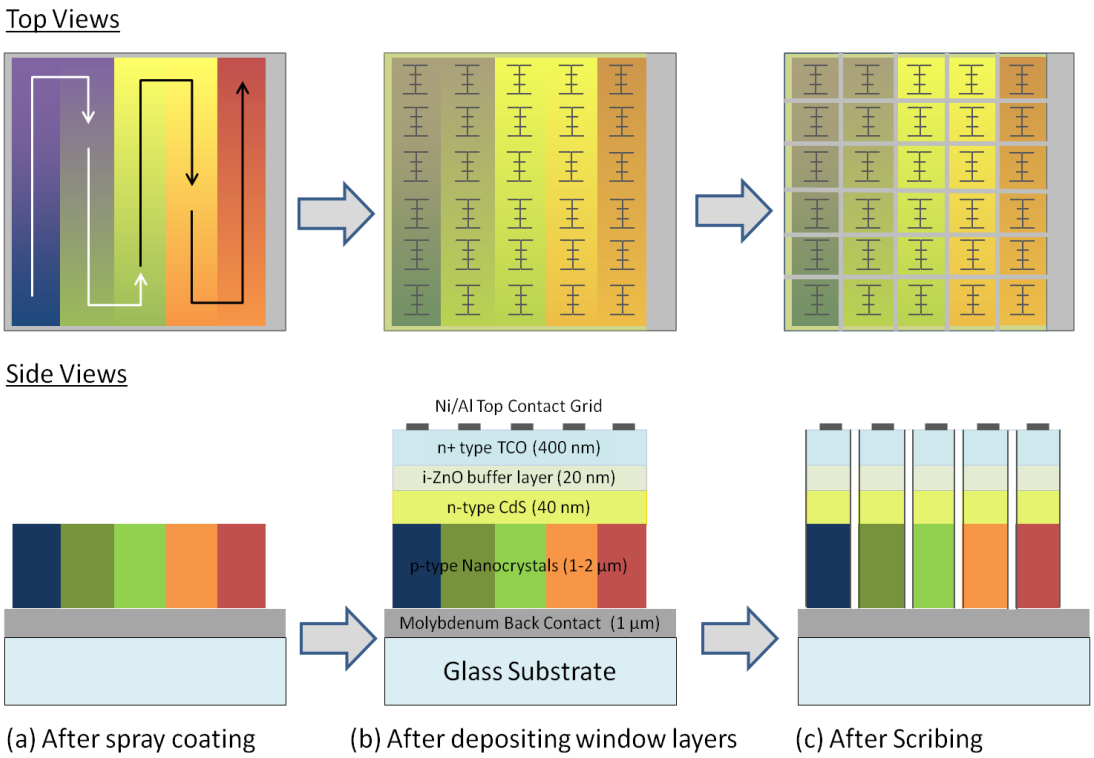

Figure 2. Schematic showing the use of the combinatorial spray-coating system to explore a large number of compositions for ink-based CZTSSe thin film solar cells. The top row is a top-view while the bottom row is a side view.

The project objectives and milestones of the effort as articulated in the SOPO were:

(1) Set-up and test a novel high-throughput ultrasonic spray coating thin film deposition platform for exploring the composition space of solution-processed chalcogenide solar cells. Current solution coating techniques allow only for uniform composition across the substrate formed with a single ink. After the project, we will be able to spatially pattern a substrate with thousands of different compositions. These are addressed in Tasks 1-2. Milestone 1 was the proof of concept of the combinatorial spray coating platform to be demonstrated by spraying compositionally graded films.

(2) Develop back surface field technology for CZTS-based devices similar to the effects of gallium in CuInGaSe2 to direct minority carriers away from the back contact. This is addressed in Task 3. Milestone 2 was to achieve 15% efficient devices using germanium alloying, Cu2Zn(Sn1-x,Gex)(S,Se)4.

(3) Discover new extrinsic doping strategies to passivate active Shockley-Read-Hall recombination centers in solution-processed CZTS-based thin film solar cells. Currently, sodium addition has been shown by many groups to dramatically reduce the SRH recombination in CIGS cells. Here we use the high-throughput

approach here to generate thousands of different compositions of extrinsic doping. We test the spatially patterned substrates with photoluminescence to examine which doping strategies minimize SRH recombination and maximize band-band recombination. This is addressed in Task 4. Milestone 3 was to achieve 20% efficient Cu2Zn(Sn1-x,Gex)(S,Se)4 devices from defect passivated absorber layers.

(4) Develop a sub-bandgap absorption model and absolute intensity photoluminescence methods to determine quasi-Fermi level splitting and characterize the effects of tail states. This was added as an expansion of the project after year 2 and was the focus of Task 5.

3. Project Results and Discussion

Task 1: Set-up of Liquid Delivery System for Ultrasonic Spray Coating

Task 1 was completed and achieved the expected outcome. The ultrasonic spray coater is completely contained inside a controlled atmosphere glovebox, is mounted above a hot plate, and is computer controlled with x-y patterning with a line width of less than 3 mm. The spray coater is configured to receive a liquid feed from an array of 6 syringe pumps that are computer controlled to set the desired mixture composition. A custom 6-way mixer with low dead time was fabricated and mounted just above the ultrasonic spray coater head.

We developed a flow injection model to determine the concentration profile that is sprayed. The capability to accurately predict the final film composition as a function of position is necessary to the mapping experiments in Tasks 2 and 3. Modeling the composition distortion of a fluid eluting from a small tube has been extensively studied due to its importance high performance liquid chromatography. Models must account for both axial and radial components of both diffusion and convection, and no single analytical model can describe all possible flow conditions that may exist. However, after modifying our liquid delivery system, we are in a regime that is exactly modeled by Gill and Ananthakrishnan result, which makes prediction of the composition gradient possible. Initial results comparing the Gill and Ananthakrishnan model with experimental composition profiles for a PEG film containing blue and yellow food dyes is shown in Figure 3. Experimental data points were collected by dicing a glass plate with a serpentine spray pattern and measuring the absorbance of dye on each piece of glass using an integrating sphere. Note the excellent agreement between the model and the measured spectroscopic data. Control using three different injectors is shown in Figure 4. Using the same control program, one may spray CZTS ink solutions by using sequences of liquid pulses from our liquid delivery system. This is the first instrument of its type that we know of, and certainly the only one that has been developed for thin film PV.

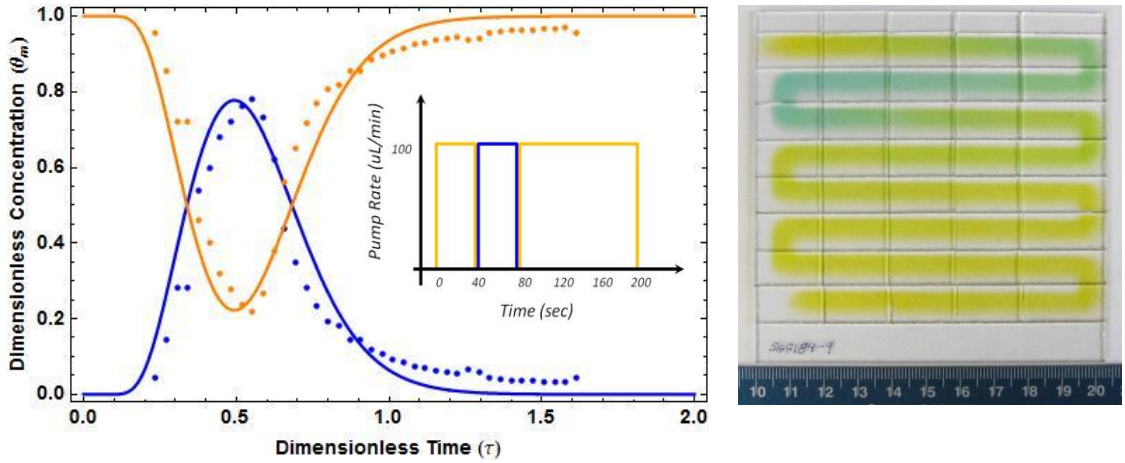

Figure 3. A dimensionless plot of dye concentration vs. time for a plate sprayed using the inset pumping program. Measured compositions are shown as points and the modeled compositions are shown as solid curves. Colors of all points and curves correspond to the dye colors they represent (i.e. yellow or blue). A photograph of the diced glass plate corresponding to the experimental data points is shown at the right. The pumping program profile and the measured dimensionless composition profile differ in shape due to flow dispersion in the liquid delivery lines. The solid curves are computed from the Gill and Ananthakrishnan model.

Figure 4. A spray coated film of dye-loaded PEG demonstrating five primary colors along the spray line (Red-Yellow-Blue-Yellow-Red). This demonstrates the ability of the instrument to control composition along a spray line with multiple source solutions.

Task 2 - Variation of Stoichiometry within the Cu2ZnSn(S,Se)4 Material System

In this task we employ the combinatorial ultrasonic spray coater developed under task 1 to explore the intrinsic defect chemistry of the CZTSSe system. Initially, our plan involved mixing inks with off-stoichiometry nanocrystals to achieve different compositions gradients. However, nanocrystals with some compositions could not be synthesized repeated. This led to a revised approach along two lines of attack: (1) Explore methods to better control nanocrystal composition and make off-stoichiometric nanocrystals and (2) Use molecular inks to achieve the composition gradients. Exploration of the nanocrystal synthesis led to two papers that reveal how to control CZTS nanocrystal composition and the mechanism of the NC formation. However, use of molecular precursors proved much more robust for gradient formation (and for higher efficiency devices).

Approach 1: Development of off-Stoichiometry Nanocrystals as the Starting Inks

When we tried to prepare inks to systematically map specific trajectories through the composition phase space defined by the two ratios (Cu/(Zn+Sn) and Zn/Sn, we found that there was significant difficulty synthesizing specific targeted ink compositions (at points other than the optimum composition we had previously identified). This led us to undertake a composition control study on Cu−Zn−Sn−S NCs in which different particle size fractions were collected over a range of reaction times from various starting reagents. From this we have determined the temporal evolution of the NC ink and identified at least two distinct particle populations that form following injection: large particles containing primarily Cu and Zn, and small particles of Cu and Sn. For short reaction times, the extreme compositional heterogeneity between these size fractions makes the average ink composition highly sensitive to changes in reaction time and precipitation procedure (see Figure 5). Longer synthesis times produce more consistent inks, with higher yield, and compositions closer to that of the starting reagents. We also found that the choice of metal precursor has a minor impact on the composition of the resulting ink compared to the changes with time, even when substituting Ge precursors for Sn precursors. Using this understanding, we demonstrate the ability to produce inks with targeted off-stoichiometric compositions. We published a paper entitled “Composition Control and Formation Pathway of CZTS and CZTGS Nanocrystal Inks for Kesterite Solar Cells”[32] in *Chemistry of Materials*.

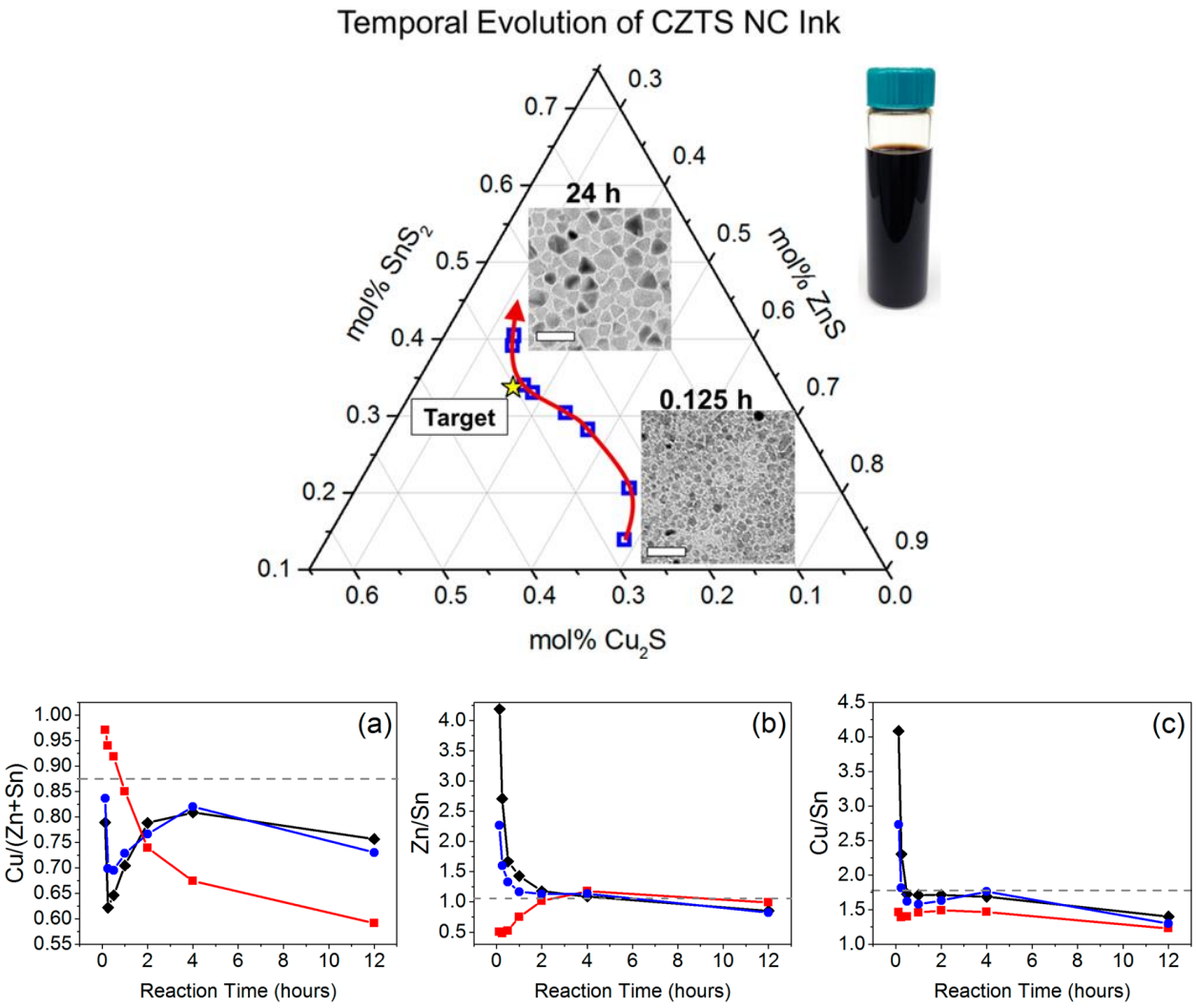

Figure 5. Top: The time trajectory of NC composition as plotted on a pseudo-ternary diagram. Bottom: The main element ratios as a function of synthesis time. For the Standard-NC (black diamonds), All-NC (blue circles), and Small-NC (red squares) fractions. The dashed line indicates the starting value for the precursors. At short reaction times, the Standard-NC fraction is Cu-poor and very Zn-rich, while the Small-NC fraction is very Cu-rich and Sn-rich. Note the extreme sensitivity to time in the early stages of growth. However, these short times are similar to most published CZTS NC syntheses.

These composition control studies have been extremely useful for us being able to hit compositions that we can then use in the high throughout experiments. As a side result, we have learned the formation pathway of the CZTS nanocrystals. In particular, we find that Cn-Sn alloy NCs and ZnS NCs nucleate first. Slowly, the copper and tin incorporate into the ZnS, gradually forming CZTS. If the reaction is stopped any time before this transformation is complete, the stoichiometry will be off in the NCs.

Further, we utilized this to study the effects that composition and NC synthesis time has on solar cell performance. Variation in reaction time produces inks with different

average size, composition, and compositional heterogeneity. Accounting for the influence of composition, we find that longer NC reaction times result in improved current collection, larger quasi-Fermi level splitting, lower defect concentrations, and higher power conversion efficiency in the sintered NC devices (Figure 6). The improvements correlate well with the measured crystalline domain size, suggesting that grain boundaries may act as non-radiative recombination sites and that effective passivation techniques may need to be developed to improve the efficiency of small-grained CZTSSe. Further, the crystalline domain size in the sintered film is proportional to the mean NC size in the ink, suggesting that some interparticle sintering occurs but that the ultimate grain size in the film is dependent on the starting NC size.

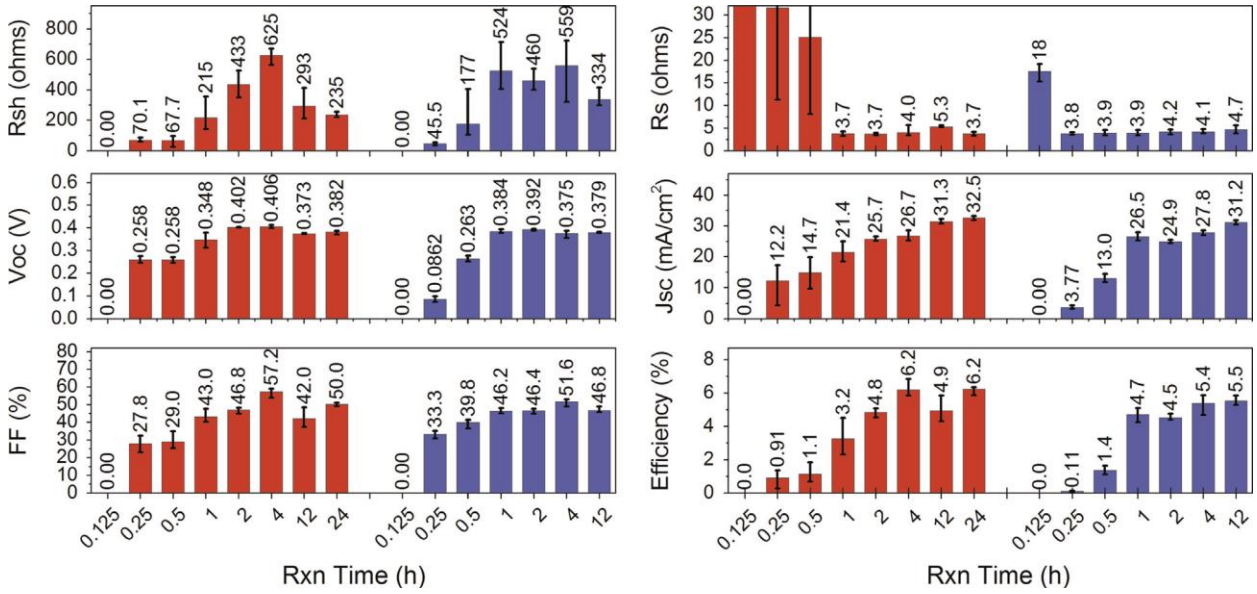

Figure 6. Parameters extracted from the current–voltage characteristic of the Standard NC devices (red) and All-NC devices (blue) with different reaction times. Error bars indicate the minimum and maximum values observed from 12 devices.

The performance of the longest reaction time devices provides the strongest evidence for the beneficial effect of reaction time. Reaction times up to 4 hours produce films with a Cu-poor/Zn-rich composition. These conditions favor the formation of benign defects and defect clusters such as [V_{Cu}+Zn_{Cu}] while suppressing the formation of more detrimental defects such as [2Cu_{Zn}+Sn_{Zn}], Sn_{Zn}, and V_{Zn}.[33-35] For this reason, the most commonly reported optimum Cu/(Zn+Sn) and Zn/Sn ratios are 0.8 and 1.2, respectively.[36] However, the 12 and 24 hour devices are Sn-rich, with Zn/Sn ratios near 0.9. At these compositions we anticipate much more unfavorable defect chemistry, and yet these devices perform as well or better than the 2 hour reaction devices which have closer to “ideal” compositions. It should also be noted that these devices were processed without any sort of post-growth etching to remove impurities. For Zn-rich films, we expect the precipitation of ZnSe, which is relatively benign, but the Sn-rich devices will likely have SnSe or $SnSe_2$, which are believed to be detrimental.[37,38] This study resulted in a publication entitled “The effect of nanocrystal reaction time on

Cu2ZnSn(S,Se)4 solar cells from nanocrystal inks"[39] in *Solar Energy Materials and Solar Cells*.

Approach 2: Development of Molecular Inks for use as Starting Inks

Given the challenges of hitting specific target stoichiometries with nanocrystals in order to make well defined composition gradients, we worked to better understand the solution phase chemistry and improve the device performance of inks based on DMSO and thiourea complexes with metal salts. Our first report[40] of this chemistry was in 2011. Under this DOE contract, we revealed the importance of the sequence of molecular complexation and redox reactions in solution. In particular, $2Cu^{+2} + Sn^{+2}$ react in DMSO solution to form stable complexes composed of $2Cu^{+} + Sn^{+4}$. This is seen also from color changes in the ink solutions in Figure 7. These advances led to the fabrication of 8% efficient devices and a publication[41] in *Advanced Energy Materials*. More importantly, it established a chemistry that could be used to start with arbitrary ink compositions in order to make composition gradients.

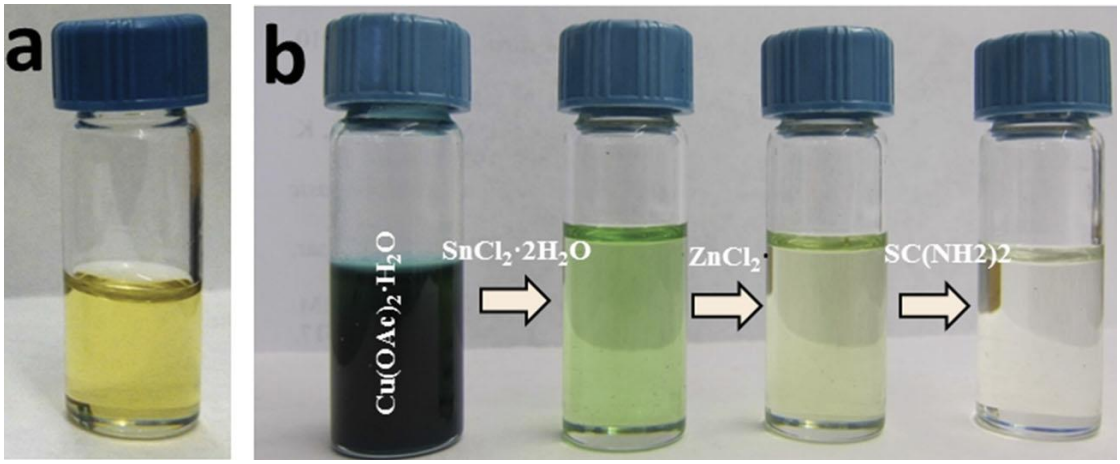

Figure 7. Photograph of (a) solution made by dissolving all precursors simultaneously in solvent and (b) solutions in each step of the precursor solution preparation. Note the difference in solution color.

Variation of CZTS Stoichiometry Using Molecular Inks

We have systematically investigated native point defect chemistry of $Cu_2ZnSn(S,Se)_4$ by spray coating films from DMSO-thiourea inks. Over 6,000 unique compositions of $Cu_2ZnSn(S,Se)_4$ have been analyzed (see Figure 8 for some of the gradient trajectories). Spectrally resolved absolute intensity photoluminescence (see Task 5) is then used to map the optoelectronic properties (see Figure 8 for an example from one gradient). The data is analyzed using a full spectrum fitting technique that allows us to extract the optical bandgap, quasi-Fermi level splitting (QFLS), and characteristics of the sub-bandgap absorption and emission. We find that changes in the optoelectronic properties primarily result from changes in the Cu-content. From stoichiometric, as the Cu-content is decreased, the PL peak shifts to higher energy, the bandgap increases, and the optoelectronic quality ($QFLS/QFLS_{max}$) increases. However, the FWHM and the

average sub-bandgap absorptivity remain nearly constant, indicating that the magnitude of electrostatic potential fluctuations does not change significantly. The most likely SRH-active defects appear to be defects and defect clusters involving Sn_{Zn}, Cu_{Sn}, and Sn_{Cu} antisite defects, particularly the cluster [$2Cu_{Zn}$ + Sn_{Zn}].

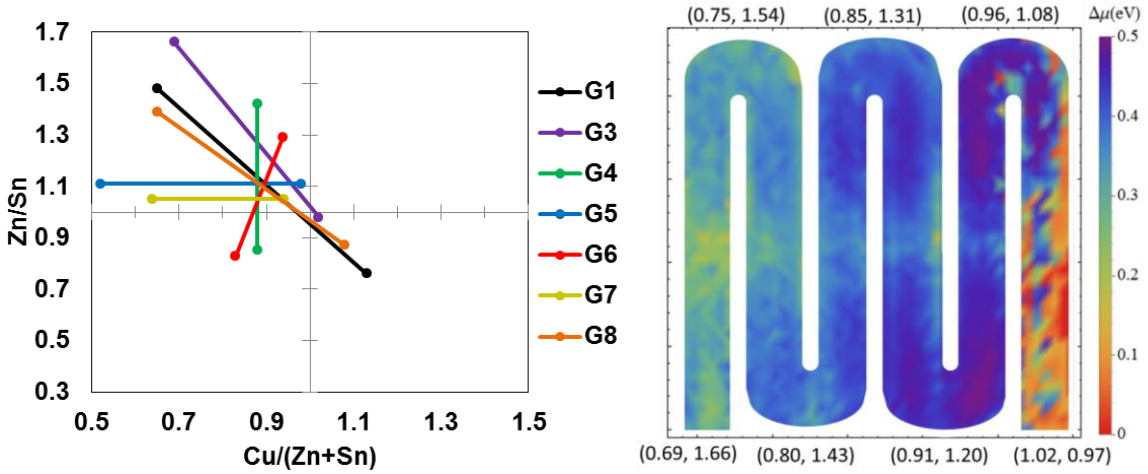

Figure 8. Photoluminescence from Composition Gradients in the CZTSSe System. Eight gradients have been analyzed thus far. The figure on the left shows how the gradients correspond to the composition space. A map of the quasi Fermi level splitting is show for the gradient G1 on the right.

Gradient G1: Broad Composition Range Screening

A broad range composition optimization was undertaken using films deposited from molecular precursor (MP) solutions. Two solutions with starting cation ratios of (0.6, 1.6) and (1.05, 0.95) where prepared and then combinatorially mixed in the ultrasonic spray coater. The presence of a gradient was confirmed using EDS and the approximate composition ratios at the endpoint of each line is shown on the extracted parameter maps (Figure 9). Figure 10 shows the extracted parameter maps for this composition gradient. Very distinct changes can be observed along the length of the spray line as the composition changes from very Cu-poor and Zn-rich to Cu-rich and Zn-poor. At compositions Cu-rich and Zn-poor, no PL emission is observed, indicating poor material quality, and thus the two right-most lines have been excluded from the parameter maps. The peak position is maximized at compositions that are much more Cu-poor and Zn-rich than devices are typically made. However, the extracted quasi-Fermi level splitting at these compositions is smaller than at compositions closer to stoichiometric and thus we would expect a lower open-circuit voltage. Both the quasi-Fermi level splitting and

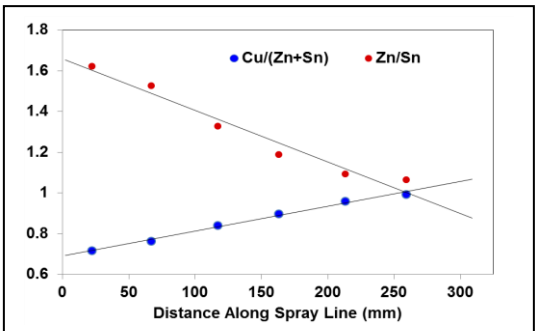

Figure 9. Composition profile of gradient G2 as determined by EDS.

the peak FWHM suggest that the best devices will be made at compositions near (0.93, 1.08), which is significantly closer to stoichiometric than the commonly reported maximum of (0.8, 1.2). This result agrees with theoretical calculations, which predict that growth under Cu-poor/Zn-rich processing conditions favors the formation of the shallow V_{Cu} acceptor and the relatively benign defect complexes [Zn_{Cu} + V_{Cu}] and [$2Zn_{Cu}$ + Zn_{Sn}] while suppressing the formation of the relatively deeper Cu_{Zn} acceptor and detrimental defect complexes such as [$2Cu_{Zn}$ + Sn_{Zn}].[33,35,42] When CZTSe is very Cu-poor/Zn-rich, the formation of V_{Cu} is favored, but as the film moves closer to stoichiometric, the formation of the relatively deeper Cu_{Zn} anti-site defects becomes preferred.[33] In addition, defect complexes such as [$2Cu_{Zn}$ + Sn_{Zn}] with sub-band edge states start to appear in greater quantity.[33] Theoretical values for the acceptor energy levels in CZTSe are 50 and 110 meV for VCu and CuZn, respectively,[43] so the redshift for this transition is expected to be small. It is most likely that the majority of the redshift is due to potential fluctuations which result from increased lattice disorder when anti-site defects and defect clusters such as [2CuZn + SnZn] are formed in greater quantity.[33]

This theory is supported by the observed intensity dependence of the peak position. At high injection levels, defects can be effectively screened by mobile charge carriers, allowing the carriers to recombine from the band edge rather than from sub-band edge defect levels, leading to a blue-shift. A smaller blue-shifting of the peak indicates smaller potential fluctuations and thus a lower concentration of defects. By varying the excitation intensity over approximately two decades, we observed that the magnitude of the blue-shift follows a similar trend to that of peak position, as described above. That is, the regions that in which the peak is the most blue-shifted to begin with exhibit the smallest blue-shift with excitation. For example, at a composition of (0.70, 1.41) the peak shifted only about 11.5 nm (9 meV) over two decades while at a composition of (0.87, 1.15) the peak blue-shifted by 25 nm (20 meV) over the same two decades. At an intermediate composition of (0.8, 1.27) the peak shifted by about 15.0 nm (12 meV).

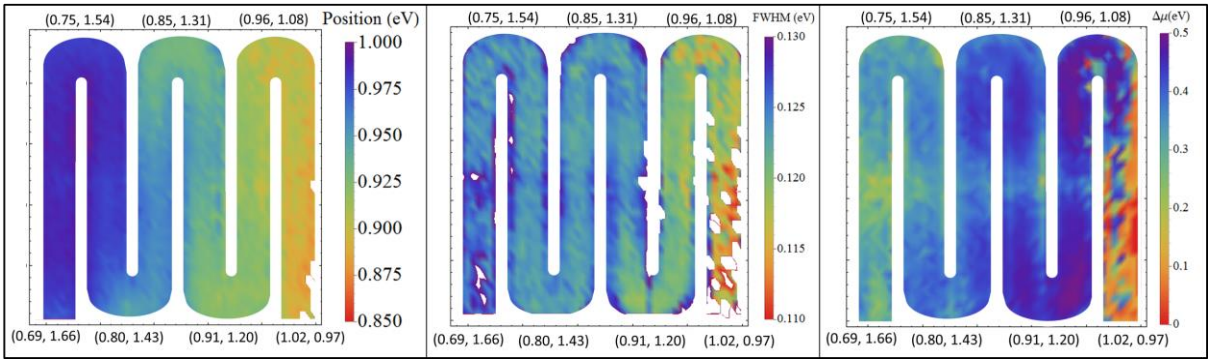

Figure 10. Extracted photoluminescence parameters from gradient G1: MP broad range screening

At Cu-poor and Zn-rich conditions, the material is so far from stoichiometric, it also leads to the precipitation of significant quantities of ZnS(e). Previous work has shown that ZnS(e) acts as a barrier to current flow[44] and that it also can be correlated with losses in open-circuit voltage.[45] We observe the latter trend in the extracted quasi-

Fermi level splitting, and thus we conclude from this gradient that the materials which will have the largest Voc are those made only slightly Cu-poor and Zn-rich.

Gradient G5: The Role of Copper content on Defect Formation

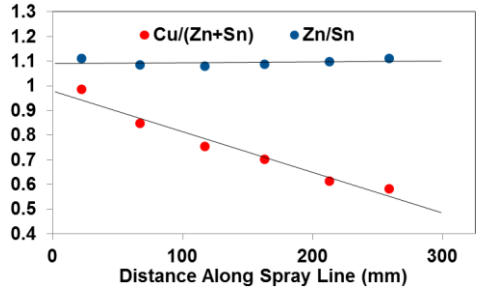

Figure 11. Composition profile of gradient G5 as determined by EDS.

The purpose of Gradient G5 (Figure 11 and 12) is to isolate the effect of the Cu/(Zn+Sn) ratio on the formation of defects by holding the Zn/Sn ratio constant. Previous work, including Gradients G1 and G2, have shown that compositions that are Cu-poor and slightly Zn-rich have the largest quasi-Fermi level splitting and the narrowest peaks (see gradients G2 and G4). For this reason a Zn/Sn ratio of 1.09 was chosen for this experiment. Holding the Zn/Sn ratio constant in the deposited film, the Cu/(Zn+Sn) ratio was varied from slightly Cu-poor (0.98) to very Cu-poor (0.52). The extracted PL parameters are shown in Figure 20. Similar to Gradients G1 and G2, we see that the most Cu-poor compositions have the highest energy peak positions but the broadest peaks and small quasi-Fermi level splitting. When the film is extremely Cu-poor, we expect the detrimental mid-gap defect Sn_{Cu} to be prevalent. Binary compounds such as ZnS(e) and SnS(e) are also likely to be abundant. ZnS(e) will simply act as a barrier to current flow, but SnSe has a smaller bandgap and thus will behave as a SRH recombination site. Compositions which are only slightly Cu-poor have the lowest energy peak positions, but the narrowest peaks and the largest quasi-Fermi level splitting, indicating that improvements in Voc may be had by processing the film closer to stoichiometric. Compositions which are only slightly Cu-poor and Zn-rich have sufficient variation in the cation ratios to favor the formation of benign defects, but do not lead to the presence of large quantities of binaries or a very high degree of compensation. When the material is highly compensated, potential fluctuations will result, and these lead to losses in open-circuit voltage/ quasi-Fermi level splitting. These result positively indicate that the copper content plays a direct role in defect formation and thus in the determination of the open-circuit voltage.

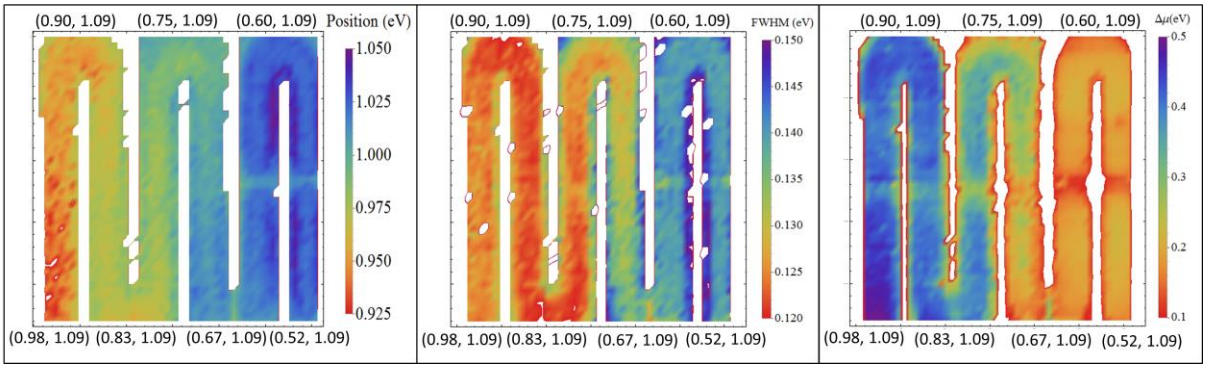

Figure 12. Extracted photoluminescence parameters from gradient G3

Gradient G4: The Role of Zinc Excess on Defect Formation

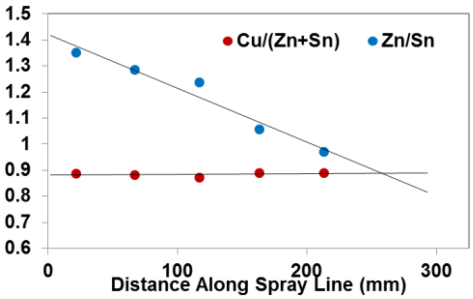

Figure 13. Composition profile of gradient G4 as determined by EDS.

Composition gradient G4 shows the effect of the Zn/Sn ratio on defect formation (Figure 13 and 14). The gradient has a constant Cu/(Zn+Sn) ratio of 0.88, but a Zn/Sn ratio which varies from Zn-rich (1.42) to Zn-poor (0.85). The extracted PL parameters are shown in Figure 22. In these maps, it can be seen that the most Zn-rich compositions have the highest energy peak positions but broad peaks and relatively lower quasi-Fermi level splitting. As the Zn/Sn ratio decreases, the peak position shifts to lower energy and the peak narrows up until close to stoichiometric. When Zn/Sn < 1, the peak position rapidly begins to decay, the peak starts to broaden, and the quasi-Fermi level splitting becomes inhomogeneous and small. From these maps we conclude that the best quality materials are made those made only slightly Zn-rich (Zn/Sn = 1.05), a result which is in contrast to the commonly stated optimum Zn/Sn = 1.2. Interestingly, films grown with too much Zn-excess show lower quasi-Fermi level splitting, indicating that too much excess Zn leads the formation of defects. This result agrees with previous work which has shown that the presence of excess ZnS decreases the open-circuit voltage.[45,46] By comparing with Gradient G3, we can see that both Zn-excess and Cu-deficiency lead to blue-shifting of the peak position, but that too much of either will lead to losses in open-circuit voltage. By comparing the magnitude of the quasi-Fermi level splitting between gradients G3 and G4, we see that the film is much more tolerant of excess zinc than it is of either copper deficiency or excess. This observation agrees with our current understanding of the defect chemistry. Excess zinc will lead to the precipitation of ZnS(e) which reduces the quasi-Fermi level splitting, it will also lead to Zn anti-site defects, such as Zn_{Sn} and Zn_{Cu}, neither of which forms a deep level defect. Together [$2Zn_{Cu}$ + Zn_{Sn}] forms a relatively benign defect complex, however large quantities of these compensated defects will cause potential fluctuations, which will have a negative impact on open-circuit voltage.

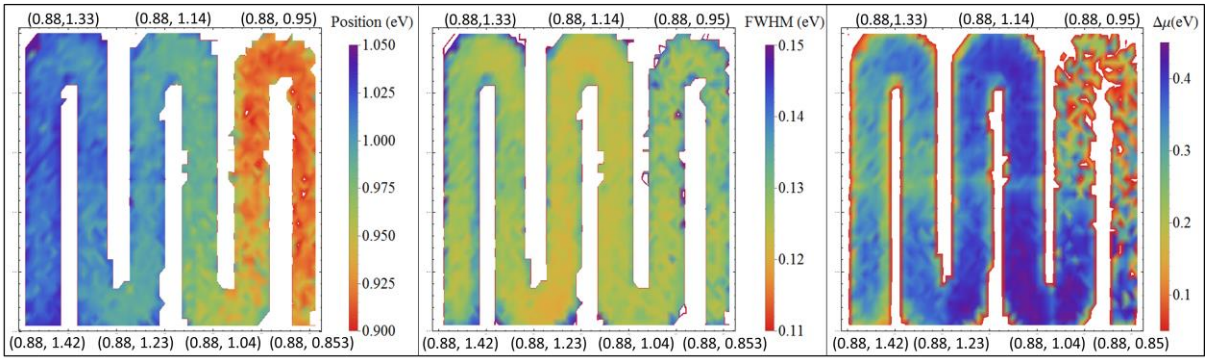

Figure 14. Extracted photoluminescence parameters from gradient G4

Gradient G7: Devices from a Copper Gradient

Gradient G7 has a composition gradient very similar to that of Gradient G5. The Zn/Sn ratio was held constant at 1.05 as the Cu/(Zn+Sn) ratio was varied from very Cu-poor (Cu/(Zn+Sn)=0.65) to approximately stoichiometric (Cu/(Zn+Sn)=1.02). The measured open-circuit voltage of the devices is shown in Figure 16. A trend of decreasing Voc is observed as the composition of the film moves from Cu-poor to Cu-rich. A region of poor open-circuit voltage between device number 10 and 30 is observed which does not follow the expected trend. The corresponding shunt resistances in this region are low (Figure 17) indicating that the device performance is limited by poor film quality; a conclusion supported by visual inspection of the film.

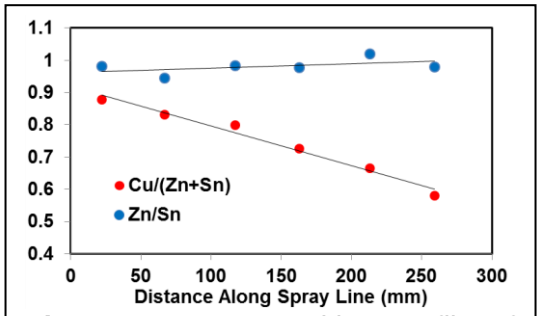

Figure 15. Composition profile of gradient G6 as determined by EDS.

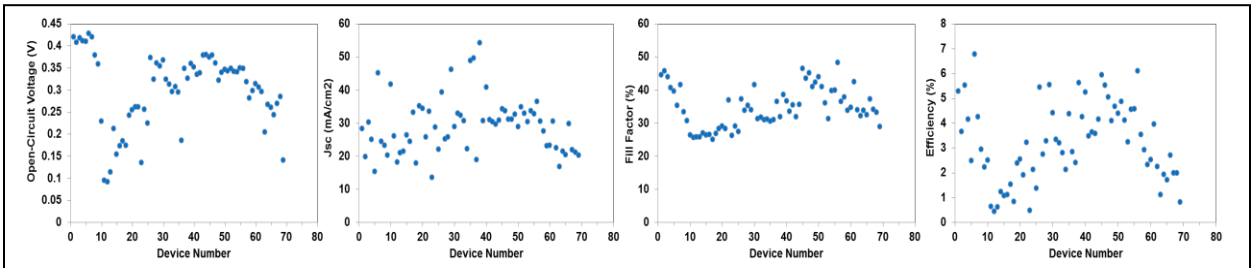

Figure 16. Measured device parameters from Gradient G6

Photoluminescence analysis was also performed on the devices. The extracted quasi-Fermi level splitting is shown in Figure 17 along with the measured open-circuit voltage. The results agree quite well, except in the region 10 through 30, where the low shunt resistance of the devices restricts the Voc. Here, the device performance is not limited by the intrinsic material quality but rather the film quality. ***This example perfectly illustrates the power of our high-throughput screening process. PL allows us to evaluate the material quality without the additional complications of device making.*** This data also further verifies that our PL calibration is correct; the extracted quasi-Fermi level splitting that we obtain does accurately reflect the open-circuit voltage that we would obtain from a device. Even though there is obviously a problem with devices 10 through 30, based on the quasi-Fermi level splitting, we would expect these devices have the highest open-circuit voltages, which is the result we expect from previous gradients.

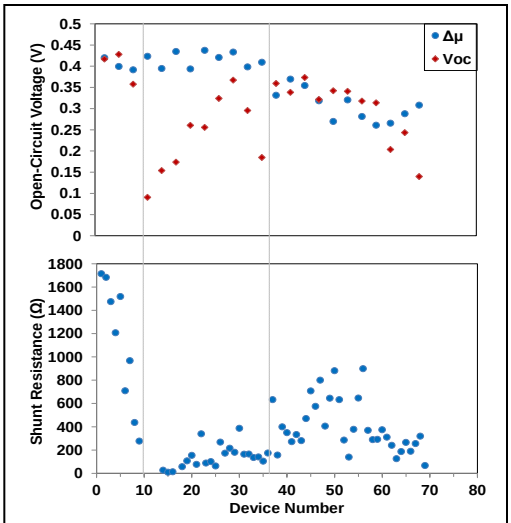

Figure 17. *Top*: Comparison of the measured open-circuit voltage to the extracted quasi-Fermi level splitting. *Bottom*: measured shunt resistance of the sprayed devices

Gradient G8: Devices from a Broad Range Gradient

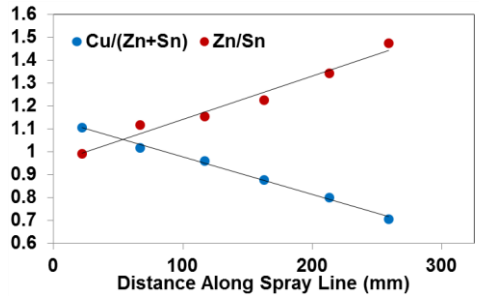

Figure 18. Composition profile of gradient G7 as determined by EDS.

After the testing of several gradients, significant improvements were made to the processing of spray lines into devices. One of the most important features was the implementation of a new high-density contact grid. A picture of the sample from Gradient G8 with this new contact grid is shown in Figure 19. Also shown in Figure 18 is the composition profile determined using EDS. This gradient is very similar to that of Gradients G1 and G2; the spray line starts Cu-rich and Zn-poor (1.10, 0.98) and gradually transitions to a composition that is very Cu-poor and Zn-rich (0.71, 1.47). Following final processing, the devices were tested under simulated AM1.5G illumination. The measured open-circuit voltage agrees very well with the extracted quasi-Fermi level splitting as shown in Figure 20. This again validates our measurement of quasi-Fermi level splitting, and shows that we can effectively predict the open-circuit voltage without having to make devices. The composition of maximum device performance, also agrees well with that determined in all of our previous gradients. All other device parameters are summarized in Figure 21. When the composition is Cu-rich and Zn-poor or close to stoichiometric, the devices perform very poorly by all metrics. As the film starts to become significantly Cu-poor and Zn-rich a rapid improvement in device parameters is seen leading to a peak in performance near the composition (0.93, 1.15). Beyond this point, the performance begins to slowly degrade as the film continues to become more Cu-poor and Zn-rich. This result agrees well with our current understanding of defects. Cu-poor and Zn-rich processing favor the formation of defects which are not detrimental, as mentioned above. When the film is processed far from stoichiometry, we expect the precipitation of binaries (specifically ZnS(e)), which will cause losses in Jsc. We also expect the material to become more heavily compensated, leading to larger potential fluctuations and thus losses in Voc.

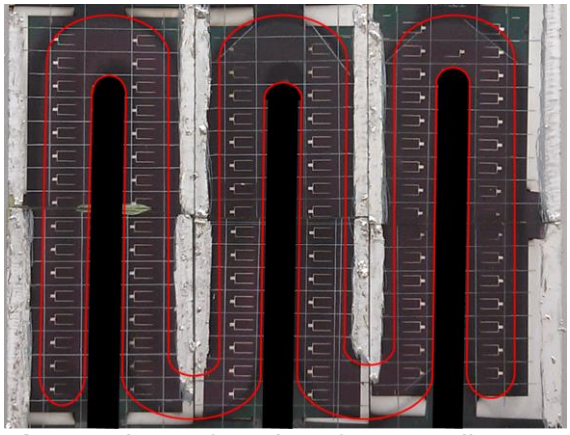

Fig 19. Photo of Devices from Gradient G8.

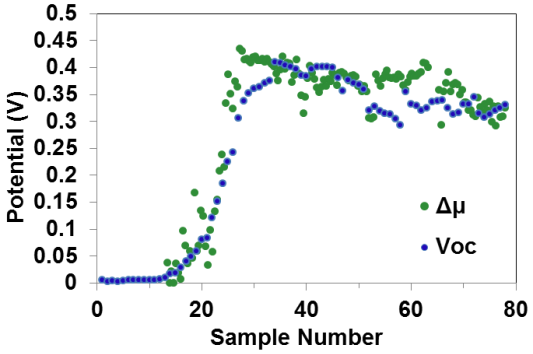

Figure 20. Measured open-circuit voltage from devices and extracted quasi-Fermi level splitting from PL for Gradient G8.

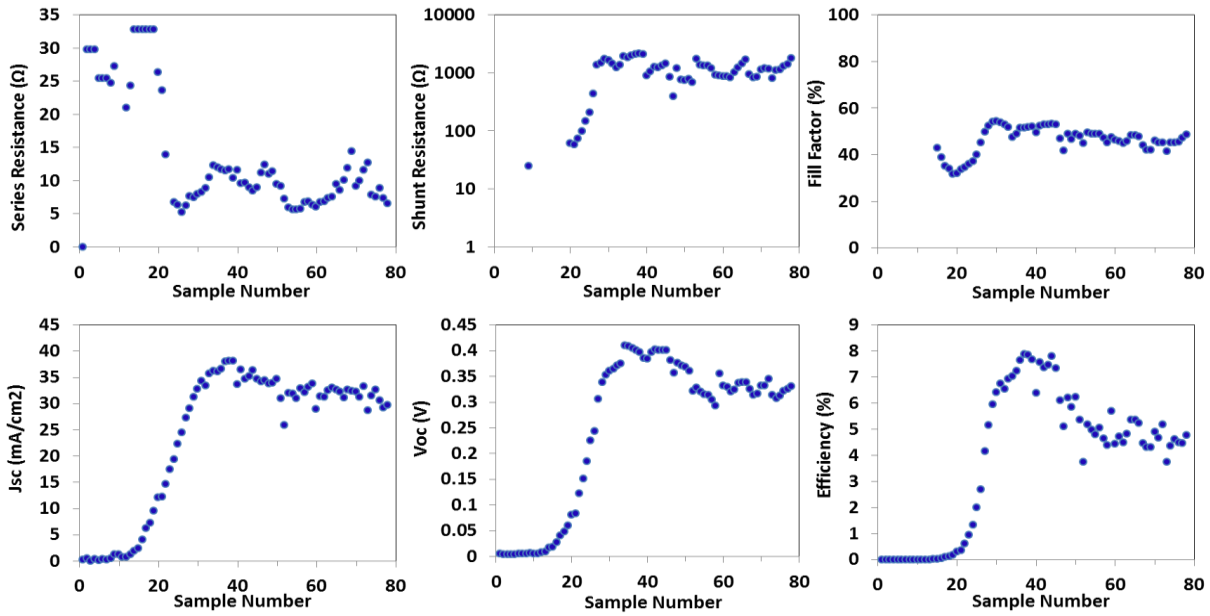

Figure 21. Measured device parameters from Gradient G8

These gradients as well as many other are summarized with regard to their effect on the quasi-Fermi level splitting in Figure 22.

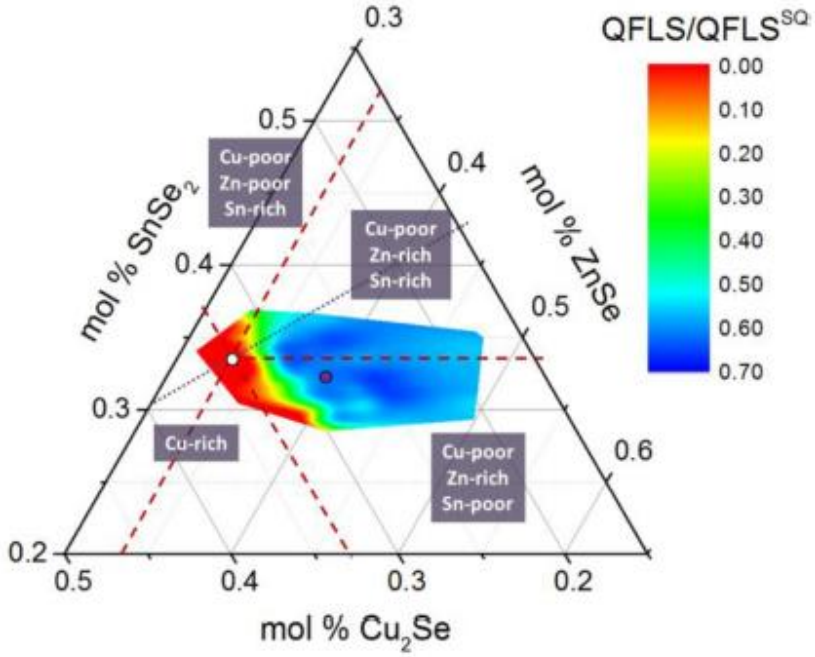

Figure 22. Map of QFLS/QFLS,max for CZTSSe. The white dot is stoichiometric, and the purple dot is the commonly believe optimum with Cu/(Zn+Sn) = 0.8 and Zn/Sn = 1.2.

Figure 22 shows that one should be able to obtain 0.69 of the maximum theoretical QFLS in CZTSSe (from spray coating DMSO-thiourea molecular precursors). Note that this is higher than the ratio of the measured open circuit voltage to theoretical limit observed even in the record 12.6% efficient CZTSSe devices from hydrazine reported by IBM, which is 0.57. ***This suggests that the Voc still has significant room for improvement, even without changes to the material itself***. While this is very positive, there is still a gap with respect to high efficiency devices from other materials. For instance the ratio of the measured Voc to theoretical Voc in 28.8% GaAs devices, 25.0% c-Si devices, 20.4% CIGSe devices, and 19.6% CdTe devices are 0.96, 0.80, 0.82, and 0.75, respectively. Please see the journal article for more details. These experiments and other were detailed in a publication[47] in the *Journal of Photovoltaics*.

Task 3 - Exploring Germanium Substitution for Tin to Direct Minority Carrier Flow

One method for increasing the band gap of kesterite materials is to alloy with germanium, forming $Cu_2Zn(Sn_xGe_{1-x})Se_4$. By doing this the bandgap can be continuously varied from about 1.0 to 1.5 eV,[48,49] the optimum range for photovoltaic devices. Analogous to gallium alloying on the indium site in CuInSe2,[50] germanium alloying on the tin site in $Cu_2ZnSn(S,Se)_4$ may also provide a means to reduce the defect density and create a back-surface field.[49] However, the Ge-containing kesterites, have been much less studied than their tin-containing relatives. This may be partly due to a perception that germanium is a less viable material for earth-abundant PV. Germanium is not a primary metal like tin, but rather a by-product of zinc production.[51] However, both Ge and Sn have similar abundance in the earth's crust. U.S. Geological Survey notes that "the amount of germanium potentially recoverable from coal fly ash is essentially unlimited", but demand for germanium has been too weak to prompt large-scale production from coal ash.[51]

In this task, we show that Ge substitution can also be used to tune the band edge alignment, improve carrier collection, and decrease the open circuit voltage deficit that has hindered kesterites. Using a simple molecular ink, we spray coat continuous composition gradients of Cu2Zn(Sn,Ge)(S,Se)4 spanning 0-90% Ge/(Ge+Sn), see Figure 23. We map the absolute intensity photoluminescence and extract the quasi-Fermi level splitting[27] (QFLS) under illumination of the bare absorber layer and completed devices. Comparing these two reveals the effects of Ge on optoelectronic quality and isolates the effects of band alignment. We also compare these data to measured open circuit voltages from photovoltaic devices fabricated from these gradients. We find that Ge can be used to increase the bandgap as high as 1.3 eV (50% Ge/(Ge+Sn)) without any loss in optoelectronic material quality and increase the device efficiency. Beyond 50% Ge/(Ge+Sn), the device efficiency decreases rapidly. We show that the degradation results from both unfavorable band alignment and a deep defect located near 0.8 eV above the valence band. However, aging the completed devices for one month in the ambient laboratory environment, the deep defect heals, and the Voc improves by as much as 227 meV. We demonstrate an 11% efficient spray coated CZTGSSe device, without anti-reflective coating, that achieves 63% of the theoretical Voc as compared to the 58% for the current record device.

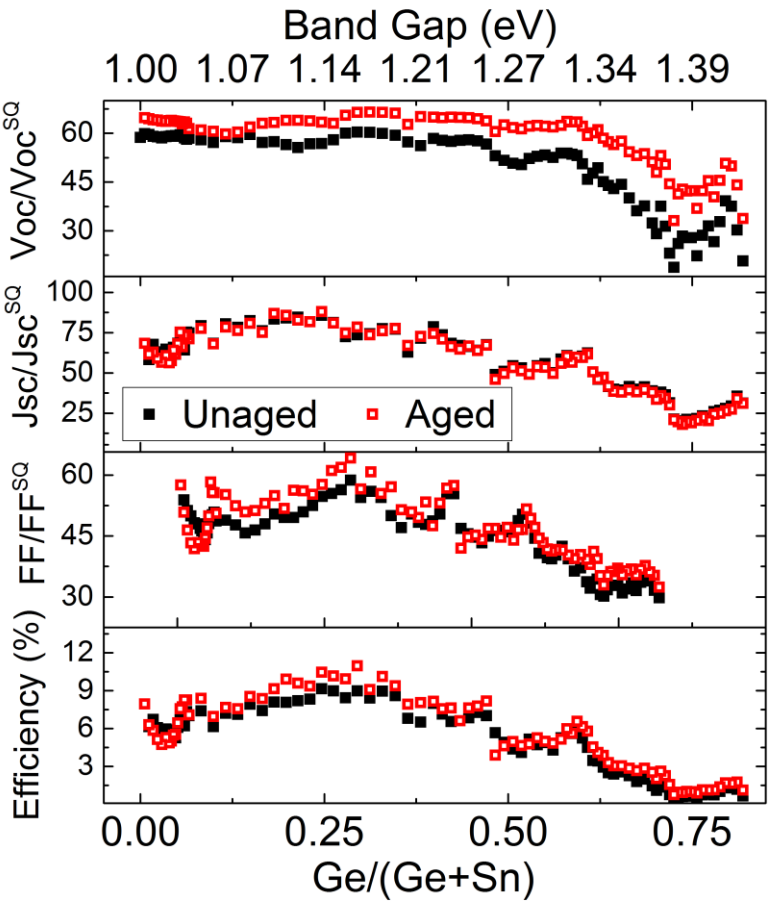

Figure 23. Current-voltage parameters before and after the sample was aged in the ambient lab environment. All values are normalized to the theoretical limit for the band gap. The bandgap was determined from the long-wavelength EQE decay.

Impact of Ageing: After allowing the completed devices to sit in an ambient lab environment for one month, we see dramatic changes in the materials properties. The AIPL at select compositions before and after ageing are shown in Figure 24. The low energy peak previously observed at higher Ge concentrations can no longer be detected. Even in the spectra without the 0.8 eV peak, we observe a significant blue-shifting of the peak, and an increase in the quasi-Fermi level splitting. The increase in the QFLS is commensurate with an increase in the open-circuit voltage as measured from the aged devices.

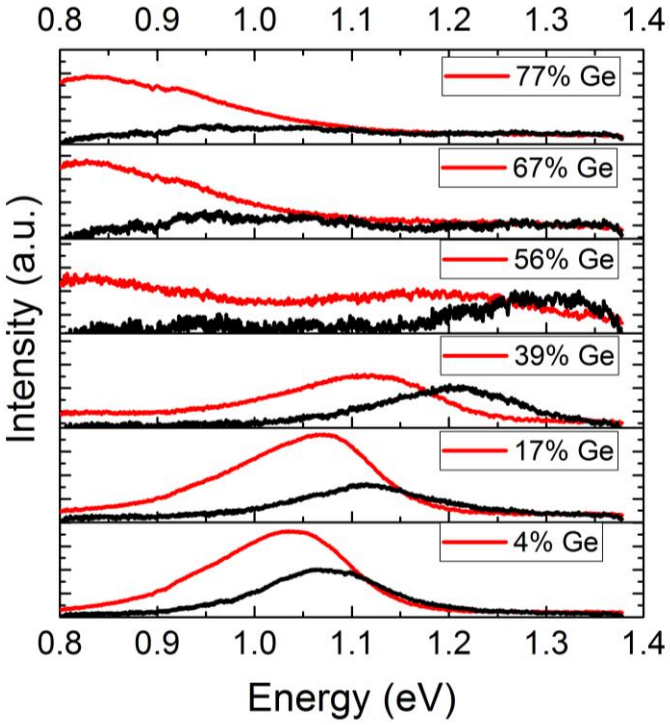

Figure 24. AIPL spectra before (red) and after (black) ageing in ambient for 1 month.

As shown in Figure 23, the aged devices show large gains in the Voc, FF and consequently in the overall power conversion efficiency. The gains in Voc increase with Ge content, reaching values as large as 227 meV for a 70% Ge device. Despite the improvements, the highest efficiency devices are still located near 25% Ge, and the decay in efficiency still occurs near 1.3 eV. The aged device has the highest power conversion efficiency of any previously published Ge-containing kesterite (11.0%), and produces 63% of the maximum Voc (Voc^{SQ}), a value higher than that of even the record 12.6% CZTSSe device (58%). However, the device suffers from a high series resistance (1.34 ohm cm^2) leading to the relatively low fill factor. If the FF could be improved to 65%, a reasonable value for good kesterite devices, the device efficiency would increase to 12.8%, without an anti-reflective coating, the highest value for any kesterite device.

Based on the above data, there are at least two primary causes for the decrease in material quality when Ge/(Ge+Sn) is greater than 50%: (1) unfavorable band alignment or (2) an increasingly deep defect. The AIPL data provides the strongest evidence for an unfavorable band alignment at higher bandgap. Comparing the QFLS before and after deposition of CdS/i-ZnO/ITO clearly shows that the QFLS in the completed device decreases with increasing band gap while the QFLS of the absorber layer alone increases with bandgap. Similarly, looking at the plot of the Voc/Voc^{SQ} vs band gap (Figure 23), we see that the highest Voc/Voc^{SQ} values occur when Eg < 1.30 eV. After about 1.30 eV the Voc quickly decays, even after ageing. These values are very similar to what has been observed with Ga-grading in CIGS.[52,53] The band positions of CIGS and CZTSe are predicted to be very similar,[34] and as with Ga-alloying in CIGS, Ge-alloying in CZTSe is expected to primarily increase the CBM, while leaving the VBM

almost unchanged.[34] Therefore, the conduction band minimum (CBM) in a material with a band gap of 1.3 eV would be about 0.3 eV higher than that of the pure selenide material. UPS measurements have shown that the band alignment between CZTSe and CdS is a spike with an approximate conduction band offset (CBO) of about +0.3-0.4 eV.[54,55] Therefore, as the Ge-content is increased, the CBO should transition from spike-like to cliff-like, near 1.3-1.4 eV. The decrease in the Voc/Voc^{SQ} starts in this range, and thus may be explained by an increasingly cliff-like band offset. Previous work has shown that a cliff-like offset reduces the maximum possible Voc from the device, and makes the device more sensitive to surface states at the absorber/buffer interface.[52] Initially, we suspected that the low energy peak observed at higher Ge concentrations could be the result of tunneling recombination from the CdS to the VBM (or acceptor states) in the CZTGSSe. To test this hypothesis, we mapped the photoluminescence at different stages of device processing, and found that the low energy peak is present even when no CdS is present. Thus the low energy PL peak must result from defect states entirely within the CZTGSSe or on the surface.

The other primary loss mechanism is the deep defect states which produce the PL peak near 0.8 eV. Previous work has reported a 0.8 eV defect CZTSSe, with depth that increases with sulfur content.[56-58] Sulfur and germanium are predicted to have a similar effect on the band structure. Both elements increase the band gap primarily by raising the CBM. Thus similar to what has been observed with sulfur, as the CBM increases due to Ge addition, the defect moves closer to mid gap and becomes a stronger recombination site. A schematic illustrating this hypothesis is shown schematically in Figure 25. Because of the proximity to the CBM, the defect likely is not beyond the demarcation level in CZTSe (the energy level where a CB electron, once captured, is equally likely to be emitted back into the conduction band or recombine with a hole from the VB) and thus is not as detrimental in CZTSe as it is in CZTS or CZTGSSe. Such a defect would explain the decay in the efficiency with increasing band gap, and would be consistent with the increasingly intense 0.8 eV PL peak (Figure 3c). Further, the reduction or elimination of this defect explains the enhanced device performance after ageing since the PL peak at 0.8 eV disappears with aging as well. At this time it is unclear how the defect is eliminated and further studies are necessary, but possible explanations include: (1) oxygenation, (2) migration of charged defects under the electric field formed by the junction, or (3) diffusion of defects or defect clusters. The fact this defect exists in the sulfide, selenide, and germanium containing kesterites suggests that the defect could be related to either Cu or Zn. Based on DFT calculations the most likely defect is a Cu_{Sn} or Cu_{Ge} defect,[35,38] although Sn_{Zn} or Sn_{Cu} are possible. The Cu_{Sn} defect has a favorable formation energy near the front of the device (when the Fermi level is near the CBM), and is predicted to be increasingly favorable in larger band gap materials.[38] However, it is not clear how this defect would be eliminated with time. A chalcogen vacancy, such as V_{Se}, that is slowly oxygenated (forming O_{Se}) could also explain the behavior.

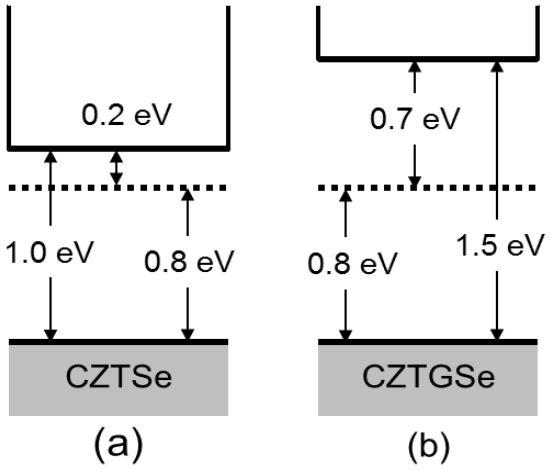

Figure 25. Schematic showing the increasing depth of a defect as the CBM is increased. Such a defect could explain the decay of the Voc with increasing Ge content.

Task 4 - Discovering Extrinsic Defect Passivation Methods

The use of extrinsic species to passivate intrinsic defects and provide shallow dopants is a crucial step in helping both CIGS and CdTe reach over 20% efficiency. Here we apply our unique high-throughput screening process to determine whether extrinsic species can be similarly used in Cu2ZnSn(S,Se)4 based solar cells. We evaluate the effect of ink-based doping of 25 different extrinsic species on the electronic and optoelectronic properties of CZTSSe absorbers and devices in concentrations ranging from 0 to 10 at% (see Figure 1 for dopants explored). We find that the absorber is tolerant of many species even at relatively high concentrations, but that certain species such as Fe, Co, and Ni are very detrimental (see Figure 26 for the example QFLS versus Co concentration). However, Li, Ge, and other elements showed interesting effects. See Task 3 for Ge studies, and see Figure 27 for the series of Group I dopants. A deeper discussion about lithium doping follows in the next section.

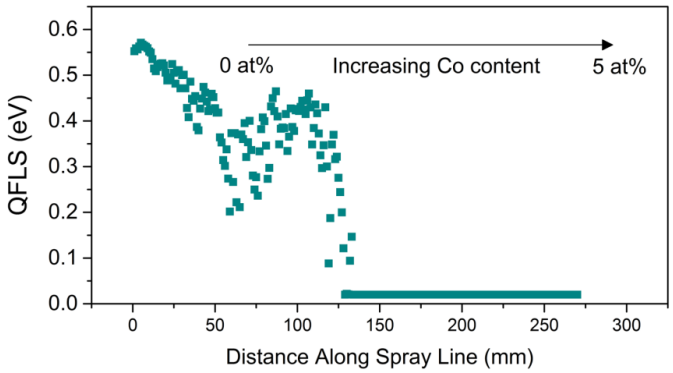

Figure 26. Measured quasi-Fermi level splitting from combinatorial spray gradients exploring the selective introduction of Co.

Further details about doping experiments is are being wrapped up and a publication is nearing completion.

Study on Lithium Doping

Given the interesting trends, we investigated the effects of lithium doping. We discovered that lithium acts to increase the p-type doping and conductivity of the film, and that it has a particularly important effect on the grain boundaries. The results of the study are published in an article entitled “Lithium-Doping Inverts the Nanoscale Electric Field at the Grain Boundaries in $Cu_2ZnSn(S,Se)_4$ and Increases Photovoltaic Efficiency” in *Physical Chemistry and Chemical Physics*.[24] A summary of the article is as follows:

Passive grain boundaries (GBs) are essential for polycrystalline solar cells to reach high efficiency. However, the GBs in $Cu_2ZnSn(S,Se)_4$ have less favorable defect chemistry compared to $CuInGaSe_2$. Here, using scanning probe microscopy we show that lithium doping of $Cu_2ZnSn(S,Se)_4$ changes the polarity of the electric field at the GB such that minority carrier electrons are repelled from the GB. Solar cells with lithium-doping show improved performance and yield a new efficiency record of 11.8% for hydrazine-free solution-processed

$Cu_2ZnSn(S,Se)_4$. We propose that lithium competes for copper vacancies (forming benign isoelectronic Li_{Cu} defects) decreasing the concentration of Zn_{Cu} donors and competes for zinc vacancies (forming a Li_{Zn} acceptor that is likely shallower than Cu_{Zn}). Both phenomena may explain the order of magnitude increase in conductivity. Further, the effects of lithium doping reported here establish that extrinsic species are able to alter the nanoscale electric fields near the GBs in $Cu_2ZnSn(S,Se)_4$. This will be essential for this low-cost Earth abundant element semiconductor to achieve efficiencies that compete with $CuInGaSe_2$ and CdTe.

Table 1. Summary of material and photovoltaic device characteristics of CZTSSe films and devices with and without LiF. The device parameters presented for each sample are average values with standard deviations from 15 solar cells with an active area of 0.10 cm^2 without antireflective coating.

LiF	Cu/ (Zn+Sn)	Zn/Sn	Eg (eV)	Jsc (mA/cm2)	Voc (V)	FF (%)	PCE (%)	n	Rs (Ω cm2)	Rsh (Ω)
No	0.74	1.14	1.08±0.023	32.2±0.6	0.426±0.011	57.8±2.6	7.93±0.47	2.25±0.16	0.53±0.11	2781±117
Yes	0.72	1.16	1.07±0.007	34.1±0.8	0.448±0.003	65.6±0.9	10.04±0.35	1.84±0.05	0.38±0.02	4095±54

[a] Calculated from fitting the linear portion of $(\ln(1\text{-EQE}))^2$ versus energy.

A central figure of the manuscript is shown below as Figure 28. This scanning Kelvin probe microscopy data shows how lithium completely inverts the electric fields at the grain boundaries. A sketch of the electric fields at the grain boundaries is shown as Figure 29 and the record device performance is shown as Figure 30.

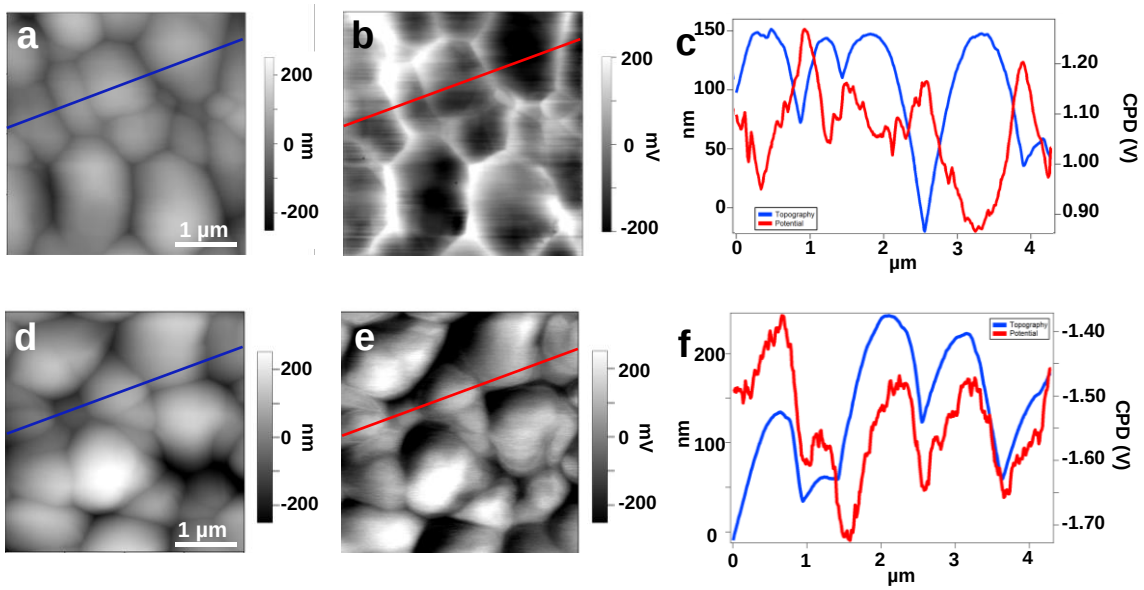

Figure 28. AFM topography images and SKPM potential maps. a,b,c, AFM topography (a), SKPM potential map (b), and plots of the topography and potential linescans of CZTSSe films without Li-doping. d,e,f, AFM topography, (d) potential map (e), and plots of the topography and potential linescans of CZTSSe films with Li-doping.

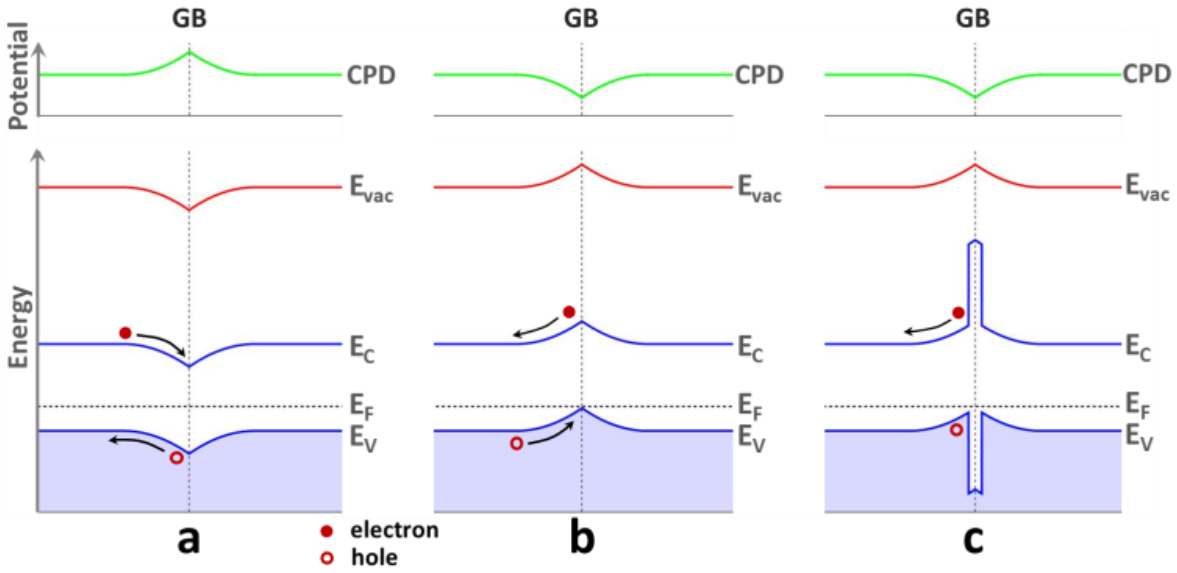

Figure 29. Diagrams across a gain boundary (GB). (a) A positive spike in the CPB at the GB, which is observed for films with no lithium. (b) A dip in the CPD at the GB assuming constant bandgap. (c) A dip in the CPD at the GB along with the formation of a higher bandgap material at the GB. Li-doped films show a dip in the CPD at the GB as shown in panel (b) and (c). However, SKPM cannot distinguish between (b) and (c). The high bandgap material at the GB in part (c) is hypothesized to be Li_2O, Li_2Se, $Li_2ZnSnSe_4$, Li_2SnO_3, SnO_2 or similar compound.

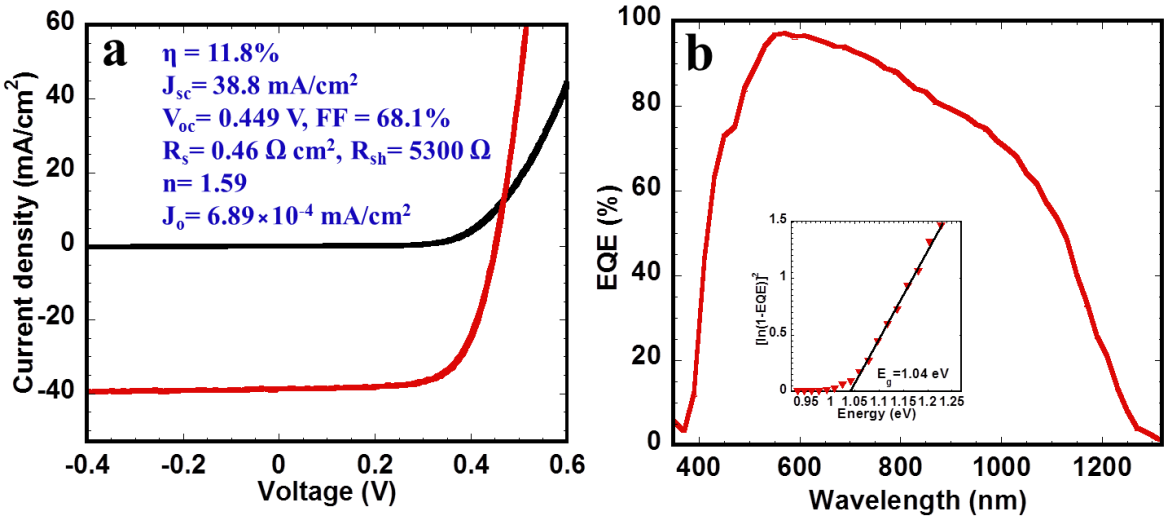

Figure 30. (a) J-V characteristics of the champion CZTSSe solar cell measured in dark and under AM 1.5 simulated sunlight. (b) External quantum efficiency (EQE) of the solar cell. Inset: Extrapolation of the bandgap from the EQE data.

Task 5. AIPL, Tail States, and Potential Fluctuations

We originally planned on using photoluminescence as a screening tool as part of Task 2. However, as we began to analyze the PL from CZTSSe, we observed that it was significantly red-shifted from the measured bandgap. One hypothesis was that it was from a quasi-donor acceptor pair. However, there were no unified theories with the above bandgap absorption that one could use to quantitatively test this theory. The sub-bandgap absorption, continuous from the bandgap, could be seen in UV-VIS_NIR absorption data. Also, the slow decay in the long wavelength EQE suggested that the origin of the red shift was a continuous decrease in absorption coefficient away from Eg. Again, there were no models in existence that we could use to see how certain sub-bandgap distribution would affect PL. So, we developed a new general model for sub-bandgap absorption and developed a fitting method that allows us to extract the quasi-Fermi level splitting. After project continuation in 2013, we expanded the effort and it became Task 5. The first results are reported in an article entitled “Quasi-Fermi Level Splitting and Sub-Bandgap Absorptivity from Semiconductor Photoluminescence,” published in the *Journal of Applied Physics*.[27] A summary of the publication follows below.

A unified model for the direct gap absorption coefficient (band-edge and sub-bandgap) is developed that encompasses the functional forms of the Urbach, Thomas-Fermi, screened Thomas-Fermi, and Franz-Keldysh models of sub-bandgap absorption as specific cases. We combine this model of absorption with an occupation-corrected non-equilibrium Planck law for the spontaneous emission of photons to yield a model of photoluminescence (PL) with broad applicability to band-band photoluminescence from intrinsic, heavily doped, and strongly compensated semiconductors. The utility of the model is that it is amenable to full-spectrum fitting of absolute intensity PL data and yields: (1) the quasi-Fermi level splitting, (2) the local lattice temperature, (3) the direct bandgap, (4) the functional form of the sub-bandgap absorption, and (5) the energy broadening parameter (Urbach energy, magnitude of potential fluctuations, etc.). The accuracy of the model is demonstrated by fitting the room temperature PL spectrum of GaAs. It is then applied to Cu(In,Ga)(S,Se)2 (CIGSSe) and Cu2ZnSn(S,Se)4 (CZTSSe) to reveal the nature of their tail states. For GaAs, the model fit is excellent, and fitted parameters match literature values for the bandgap (1.42 eV), functional form of the sub-bandgap states (purely Urbach in nature), and energy broadening parameter (Urbach energy of 9.4 meV). For CIGSSe and CZTSSe, the model fits yield quasi-Fermi leveling splittings that match well with the open circuit voltages measured on devices made from the same materials and bandgaps that match well with those extracted from EQE measurements on the devices. The power of the exponential decay of the absorption coefficient into the bandgap is found to be in the range of 1.2 to 1.6, suggesting that tunneling in the presence of local electrostatic potential fluctuations is a dominant factor contributing to the sub-bandgap absorption by either purely electrostatic (screened Thomas-Fermi) or a photon-assisted tunneling mechanism (Franz-Keldysh). A Gaussian distribution of bandgaps (local Eg fluctuation) is found to be inconsistent

with the data. The sub-bandgap absorption of the CZTSSe absorber is found to be larger than that for CIGSSe for materials that yield roughly equivalent photovoltaic devices (8% efficient). Further, it is shown that fitting only portions of the PL spectrum (e.g., low energy for energy broadening parameter and high energy for quasi-Fermi level splitting) may lead to significant errors for materials with substantial sub-bandgap absorption and emission.

The core theory of the method is summarized briefly: The square-root dependence of the joint-density-of-states for an ideal direct-gap semiconductor was convoluted with a model of the sub-bandgap states that is an exponential with two free parameters—one that sets the functional form of the decay away from the band edge, θ, and another that quantifies the magnitude of the energy broadening, γ. The convolution yields an expression for the absorption coefficient (excluding any state occupation effects):

$$\alpha(\Delta\varepsilon) = \frac{\alpha_0}{\gamma 2\Gamma(1+1/\theta)} \int_{-\infty}^{\Delta\varepsilon} g_{\text{tail}}(\Delta\varepsilon')\, g_{\text{direct}}(\Delta\varepsilon - \Delta\varepsilon')\, d\Delta\varepsilon' \qquad 1.$$

where:

$$g_{\text{tail}}(\Delta\varepsilon) = exp\left(-\left|\frac{\Delta\varepsilon}{\gamma}\right|^{\theta}\right)$$

$$g_{\text{direct}}(\Delta\varepsilon) = \sqrt{\Delta\varepsilon}$$

Here $\Delta\varepsilon = \varepsilon - E_g$, E_g is the direct bandgap, Γ is the gamma function (required for proper normalization of the convolution integral), and α_0 is a material-dependent parameter that characterizes the strength of the direct transition (α_0 is typically in the range of 10^4 to 10^5 $cm^{-1}eV^{-0.5}$ but depends on the oscillator strength). The use of a variable exponent, θ, allows the model to encompass the Urbach Tail model (θ=1.0),[59] the Thomas-Fermi or " Gaussian" model (θ=2.0),[60] the screened Thomas-Fermi (θ=1.25),[61] and Franz-Keldysh asymptotics (θ=1.5)[62] all as limiting cases. This absorption coefficient is used to calculate the absorptivity, neglecting effects from reflection by:

$$a(\varepsilon) = 1 - exp(\alpha(\varepsilon)d) \qquad 2.$$

Here d is the characteristic length over which photons are absorbed and excited carriers travel and recombine. By taking advantage of the reciprocity between absorption and emission,[63] we plug this absorptivity into a generalized Planck law for non-equilibrium photoemission that is a product of four factors: (1) the photon density of states for emission into the full hemisphere above the semiconductor surface, (2) Bose-Einstein distribution, (3) the spectral absorptivity, and (4) a correction factor that accounts for electronic state occupation: [27]

$$I_{pL}(\varepsilon) = \left(\frac{2\pi\,\varepsilon^2}{h^3 c^2}\right)\left(\frac{1}{exp\left(\frac{\varepsilon-\Delta\mu}{kT}\right)-1}\right) a(\varepsilon)\left(1 - \frac{2}{exp\left(\frac{\varepsilon-\Delta\mu}{2kT}\right)+1}\right) \qquad 3.$$

The fourth factor assumes symmetric quasi-Fermi level splitting from midgap and becomes important only when the energy of emission approaches $\Delta\mu$. For cases where

$\varepsilon > \Delta\mu$ by at least 8kT, the last factor is typically negligible and approaches 1 quickly for larger ε. Also, for this same energy range the "-1" in the Bose-Einstein term becomes negligible, and the PL is accurately modeled as:

$$I_{pL}(\varepsilon) = \left(\frac{2\pi\,\varepsilon^2}{h^3 c^2}\right) exp\left(\frac{-\varepsilon}{kT}\right) exp\left(\frac{\Delta\mu}{kT}\right) a(\varepsilon) \qquad 4.$$

The energy dependence from $\exp(-\varepsilon/kT)$ dominates the ε^2 factor, and one clearly sees how the PL is dominated by low transition energy states. Thus, a shift of the PL peak position to lower energy from the bandgap is a sign of the presence of sub-bandgap states. Such states cause a significant decrease in the open circuit voltage as verified by our own detailed balance (Shockley-Queisser) calculations.

The model is shown in Figures 31 where the absorptivity and calculated PL are shown for several values of theta and gamma. The application of the model to PL data from GaAs, CIGSSe and CZTSSe are shown in Figure 32.

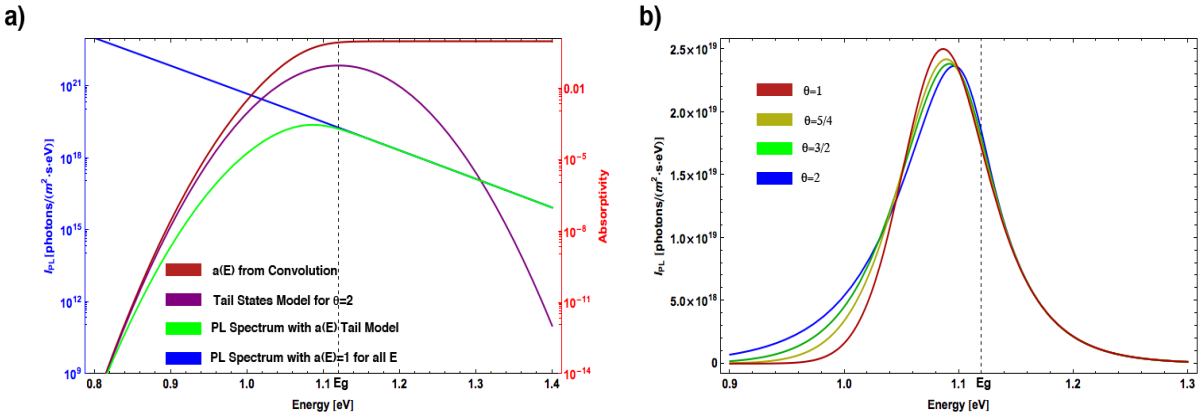

Figure 31. Photoluminescence Predicted from the General Absorptivity Model. (a) PL and absorptivity curves for θ=2. The low energy limit of the absorptivity (Gaussian tail states) and PL spectrum assuming an absorptivity of 1 for all energies are shown as well. (b) Simulated PL spectra generated for limiting cases of the exponent and T=400K, Δμ=0.5eV, and Eg=1.12eV. The γ parameter has been chosen such that the integration of sub-Eg absorptivity is 0.0371 for all cases.

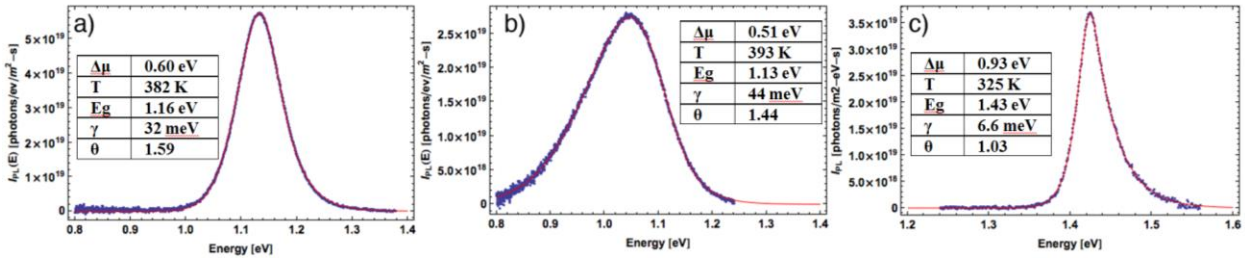

Figure 32. Full Spectrum Fitting of PL with our Model. (a) PL from a CIGSe device. (b) Same analysis but for a molecular precursor CZTSSe device from our lab. (c) Same analysis but for a doped GaAs wafer. Note the outstanding ability of the general model to fit the entire PL peaks for all three materials. We have also tested the model on simulated data (with Poisson noise) and found that the full spectrum fit robustly finds the correct quasi Fermi Level splitting and temperature.

We have also used this general model to explore the theoretical limits to efficiency in the presence of tail states. Under the assumption of quasi-thermal equilibrium, we can use our model to conduct detailed balance calculations. The results of one of those calculations and a comparison to the Shockley-Queisser limit and our experimental data is shown in Table 2 and Figure 33. ***The most important conclusion from the detailed balance calculations is that the presence of the tail states only results in a loss of 90 mV in open circuit voltage (in the radiative limit). This proves that the tail states alone are not sufficient to explain the low open circuit voltages in CZTSSe.***

	DB	DB With Tail	UW DMSO-TU
Bandgap	1.06	1.06	1.06
Efficiency [%]	32.1	29.3	11.1
J_{sc} [mA/cm^2]	45.2	46.3	36.2
V_{oc} [mV]	822	732	458
FF [%]	86.4	85.6	67.0
n	1.00	1.03	1.74
Rsh [Ω]	∞	∞	8820
Rs [Ω-cm^2]	0	0	0.415

Table 2. Comparison of device parameters from a conventional detailed balance calculation (with sharp band edge), detailed balance calculation with tails states similar to what we observe in the PL, and experimental data for our best device.

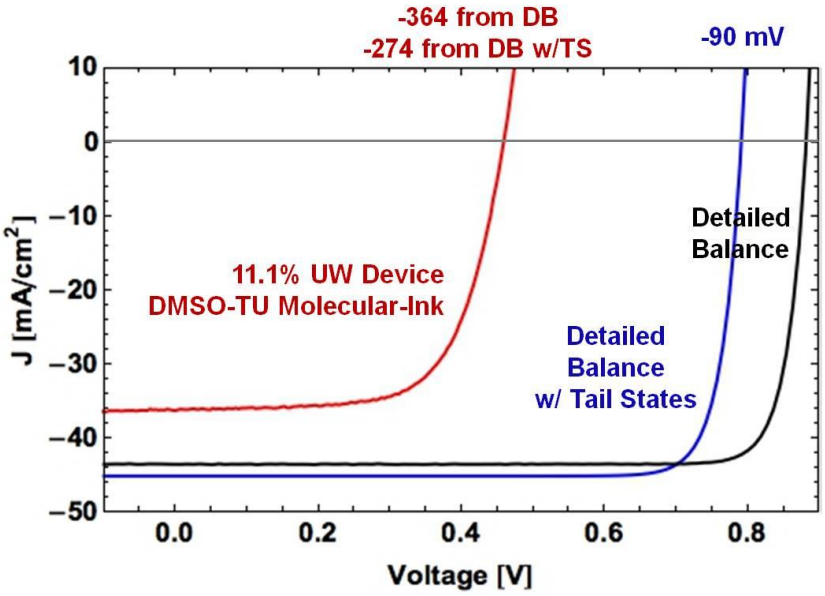

Figure 33. Comparison of current voltage curves for a conventional detailed balance calculation (with sharp band edge), detailed balance calculation with tails states similar to what we observe in the PL, and experimental data for our best device. Note that the presence of tail states results in a loss of only 90 mV in the radiative limit.

4. Conclusions

We successfully developed an ultrasonic spray coating system that can be used to deposit thin chalcogenide films with composition gradients. The instrument was used to reveal the effects of intrinsic composition and examine the effects of 25 different dopant elements. Surprisingly, doping with most elements had little to no effect on the quasi-Fermi level splitting of bare films. A few elements were found to be detrimental including Fe, Co, and Ni. However, Li, Ge, and other elements were discovered to be beneficial. Ge and Li were explored in depth, and our best devices utilize lithium doping.

In order to determine the optoelectronic quality of the absorber layers we developed a new model of absorption coefficients, that when combined with absolute intensity photoluminescence, yields the steady-state quasi-Fermi level splitting and a way to quantify the sub-bandgap absorption. This is a significant development that should impact other PV technologies. Further, the model shows that tail states (potential fluctuations) in CZTSSe can only explain about 90 mV of loss in the open circuit voltage.

By using these methods, we found that lithium doping has several beneficial effects on CZTSSe. It improves the open-circuit voltage, short circuit current, fill factor, and shunt resistance. By using scanning Kelvin probe microscopy (SKPM) and conductive AFM (along with device measurements, DLPC, and XPS), we discovered that lithium acts to increase the p-type doping in both the grain and grain boundaries (GBs). The effect is stronger in the GBs and changes the direction of the electric field at the GB. In lithium doped devices, an electric field repels minority carrier electrons away from the GB. This resulted in a publication and the fabrication of 11.8% efficient devices from a DMSO-thiourea molecular ink. The mechanism of action is most likely due to the formation of Li_{Cu}, which inhibits the formation of the donor defect Zn_{Cu}. This reduces compensation and increases the net p-type doping.

In addition, by alloying with germanium, we have fabricated CZTGSSe devices with the best open-circuit voltage (relative the maximum theoretical open-circuit voltage for the bandgap) for any kesterite solar cell. The Voc/Voc,max is 63%, compared to 58% for the record efficiency cell from hydrazine. The origin of the increased voltage efficiency appears to be related to the conduction band off-set and the suppression of a deep defect (~0.8 eV), most likely due to Cu_{Sn}, but Sn_{Zn} or Sn_{Cu} are also possible.

All milestones and go/no-go metrics were met with exception of the device efficiency milestone (15% then 20%). However, under the contract, hydrazine-free CZTSSe device efficiencies increased from 7.2% at the start of the contract to 11.8% upon completion.

5. Budget and Schedule

The approved budget and the project expenditures are summarized in the following table. All funds have been spent. There are some deviations between the planned expenditures in each budget class and the actual. In particular, the supplies category and “other” category are each over spent by about $20k. This is a result of the fact that the project was a bit more demanding in terms of chemicals, substrates, and user fees than originally anticipated. The travel category is also over spent. An estimate of $6k for yearly trips to PVSC or MRS for the PI and graduate students over the 4 year project was simply a poor estimate.

Object Class Categories **Per SF 424a**	**Approved Budget ($)**	**Project Expenditures ($)**
a. Personnel	$227,501	$176,385
b. Fringe Benefits	$45,496	$35,106
c. Travel	$6,000	$19,415
d. Equipment		
e. Supplies	$28,762	$57,618
f. Contractual		
g. Construction		
h. Other	$66,716	$86,845
i. Total Direct Charges (sum of a to h)	$374,475	$375,370
j. Indirect Charges	$167,390	$166,495
k. Totals (sum of i and j)	**$541,865**	**$541,865**

6. Path Forward

Clearly the most significant challenge to achieving high efficiency devices is overcoming the low voltages. The prevailing opinion (up to 2015) appears to be that Cu/Zn site disorder and the resulting potential fluctuations were the fundamental limitation. However, our experiments show that potential fluctuations only result in a 90 mV loss (in the radiative limit). Further, recent experiments with extended low temperature annealing that reduces Cu/Zn disorder have not shown high open-circuit voltages in high performance devices. Deep defects, particularly related to tin (Cu_{Sn}, Sn_{Zn} or Sn_{Cu}), may be the culprit. Our experiments with Ge alloying support this hypothesis. This points towards a path forward that may be used to increase the open circuit voltages even further. Further, we are applying some of the techniques developed under this proposal to CuIn(S,Se)2 and CuInGa(S,Se)2. We have recently published a paper [64] in *Energy and Environmental Science* with a new World-record for solution processed CISSe of 13.0%. The overall World-record is 15.4% by co-evaporation. We also achieved 14.7% CIGSSe. These were the first experiments with our DMSO-thiourea chemistry. We expect that these may be increased significantly. We are pursuing both the development of passivated CZTSSe and hydrazine free solution processed CISSe and CIGSSe and hope to submit a proposal to DOE in the near future.

7. References

1. Moutinho HR, Al-Jassim MM, Levi DH, Dippo PC, Kazmerski LL: **Effects of CdCl2 treatment on the recrystallization and electro-optical properties of CdTe thin films**. *Journal of Vacuum Science & Technology a-Vacuum Surfaces and Films* 1998, **16**:1251-1257.
2. Harvey SP, Teeter G, Moutinho H, Al-Jassim MM: **Direct evidence of enhanced chlorine segregation at grain boundaries in polycrystalline CdTe thin films via three-dimensional TOF-SIMS imaging**. *Progress in Photovoltaics* 2015, **23**:838-846.
3. Ringel SA, Smith AW, Macdougal MH, Rohatgi A: **The Effects of $CdCl_2$ on the Electronic Properties of Molecular Beam Epitaxially Grown CdTe/CdS Heterojunction Solar Cells**. *Journal of Applied Physics* 1991, **70**:881-889.
4. Ruckh M, Schmid D, Kaiser M, Schaffler R, Walter T, Schock HW, Ieee: **Influence of substrates on the electrical properties of Cu(In,Ga)Se-2 thin films**. In *1994 Ieee First World Conference on Photovoltaic Energy Conversion/Conference Record of the Twenty Fourth Ieee Photovoltaic Specialists Conference-1994, Vols I and Ii*. I E E E; 1994:156-159.
5. Hedstrom J, Ohlsen H, Bodegard M, Kylner A, Stolt L, Hariskos D, Ruckh M, Schock H: **ZnO/CdS/Cu(In,Ga)Se_2 thin film solar cells with improved performance**. In *Photovoltaic Specialists Conference, 1993., Conference Record of the Twenty Third IEEE*; 1993:364-371.
6. Nakada T, Iga D, Ohbo H, Kunioka A: **Effects of sodium on Cu(In, Ga)Se-2-Based thin films and solar cells**. *Japanese Journal of Applied Physics Part 1-Regular Papers Short Notes & Review Papers* 1997, **36**:732-737.
7. Pianezzi F, Reinhard P, Chirila A, Bissig B, Nishiwaki S, Buecheler S, Tiwari AN: **Unveiling the effects of post-deposition treatment with different alkaline elements on the electronic properties of CIGS thin film solar cells**. *Physical Chemistry Chemical Physics* 2014, **16**:8843-8851.
8. Chirila A, Reinhard P, Pianezzi F, Bloesch P, Uhl AR, Fella C, Kranz L, Keller D, Gretener C, Hagendorfer H, et al.: **Potassium-induced surface modification of Cu(In,Ga)Se-2 thin films for high-efficiency solar cells**. *Nature Materials* 2013, **12**:1107-1111.
9. Nakakoba H, Yatsushiro Y, Mise T, Kobayashi T, Nakada T: **Effects of Bi Incorporation on Cu(In1-x,Ga-x)Se-2 Thin Films and Solar Cells**. *Japanese Journal of Applied Physics* 2012, **51**.
10. Nakada T, Honishi Y, Yatsushiro Y, Nakakoba H: **Impacts of Sb and Bi incorporations on CIGS thin films and solar cells**. In *Photovoltaic Specialists Conference (PVSC), 2011 37th IEEE*; 2011:003527-003531.
11. Yuan M, Mitzi DB, Gunawan O, Kellock AJ, Chey SJ, Deline VR: **Antimony assisted low-temperature processing of CuIn1 − xGaxSe2 − ySy solar cells**. *Thin Solid Films* 2010, **519**:852-856.
12. Kronik L, Cahen D, Schock HW: **Effects of sodium on polycrystalline Cu(In,Ga)Se-2 and its solar cell performance**. *Advanced Materials* 1998, **10**:31-+.
13. Yan Y, Noufi R, Al-Jassim MM: **Grain-Boundary Physics in Polycrystalline CuInSe_{2} Revisited: Experiment and Theory**. *Physical Review Letters* 2006, **96**:205501.
14. Yan Y, Jiang CS, Noufi R, Wei S-H, Moutinho HR, Al-Jassim MM: **Electrically benign behavior of grain boundaries in polycrystalline CuInSe(2) films**. *Physical Review Letters* 2007, **99**.

15. Persson C, Zunger A: **Anomalous grain boundary physics in polycrystalline CuInSe2: The existence of a hole barrier**. *Physical Review Letters* 2003, **91**:4.
16. Persson C, Zunger A: **Compositionally induced valence-band offset at the grain boundary of polycrystalline chalcopyrites creates a hole barrier**. *Applied Physics Letters* 2005, **87**.
17. Todorov TK, Reuter KB, Mitzi DB: **High-Efficiency Solar Cell with Earth-Abundant Liquid-Processed Absorber**. *Advanced Materials* 2010, **22**:E156.
18. Choudhary G, Hansen H: **Human Health Perspective of Environmental Exposure to Hydrazines: A Review**. *Chemosphere* 1998, **37**:801-843.
19. Roe FJC, Grant GA, Millican DM: **Carcinogenicity of Hydrazine and 1,1-Dimethylhydrazine for Mouse Lung**. *Nature* 1967, **216**:375-376.
20. Guo Q, Kim SJ, Kar M, Shafarman WN, Birkmire RW, Stach EA, Agrawal R, Hillhouse HW: **Development of CuInSe2 Nanocrystal and Nanoring Inks for Low-Cost Solar Cells**. *Nano Letters* 2008, **8**:2982-2987.
21. Guo Q, Ford GM, Hillhouse HW, Agrawal R: **Sulfide Nanocrystal Inks for Dense Cu(In,Ga)(S,Se)2 Absorber Films and Their Photovoltaic Performance**. *Nano Letters* 2009, **9**:3060-3065.
22. Guo QJ, Hillhouse HW, Agrawal R: **Synthesis of Cu_2ZnSnS_4 Nanocrystal Ink and Its Use for Solar Cells**. *Journal of the American Chemical Society* 2009, **131**:11672.
23. Hillhouse HW, Beard MC: **Solar Cells from Colloidal Nanocrystals: Fundamentals, Materials, Devices, and Economics**. *Current Opinion in Colloid & Interface Science* 2009, **14**:245-259.
24. Xin H, Vorpahl SM, Collord AD, Braly IL, Uhl AR, Krueger BW, Ginger DS, Hillhouse HW: **Lithium-doping inverts the nanoscale electric field at the grain boundaries in $Cu_2ZnSn(S,Se)_4$ and increases photovoltaic efficiency**. *Physical Chemistry Chemical Physics* 2015, **17**:23859-23866.
25. Haass SG, Diethelm M, Werner M, Bissig B, Romanyuk YE, Tiwari AN: **11.2% Efficient Solution Processed Kesterite Solar Cell with a Low Voltage Deficit**. *Advanced Energy Materials* 2015:n/a-n/a.
26. Collord AD, Xin H, Hillhouse HW: **Combinatorial Exploration of the Effects of Intrinsic and Extrinsic Defects in $Cu_2ZnSn(S,Se)_4$**. *Photovoltaics, IEEE Journal of* 2014, **PP**:1-11.
27. Katahara JK, Hillhouse HW: **Quasi-Fermi Level Splitting and Sub-Bandgap Absorptivity from Semiconductor Photoluminescence**. *Journal of Applied Physics* 2014, **116**:173504.
28. Wang W, Winkler MT, Gunawan O, Gokmen T, Todorov TK, Zhu Y, Mitzi DB: **Device Characteristics of CZTSSe Thin-Film Solar Cells with 12.6% Efficiency**. *Advanced Energy Materials* 2013.
29. Gokmen T, Gunawan O, Mitzi DB: **Semi-empirical device model for Cu2ZnSn(S,Se)(4) solar cells**. *Applied Physics Letters* 2014, **105**.
30. Gokmen T, Gunawan O, Todorov TK, Mitzi DB: **Band tailing and efficiency limitation in kesterite solar cells**. *Applied Physics Letters* 2013, **103**:103506.
31. Gershon T, Shin B, Gokmen T, Lu S, Bojarczuk N, Guha S: **Relationship between Cu2ZnSnS4 quasi donor-acceptor pair density and solar cell efficiency**. *Applied Physics Letters* 2013, **103**.

32. Collord AD, Hillhouse HW: **Composition Control and Formation Pathway of CZTS and CZTGS Nanocrystal Inks for Kesterite Solar Cells**. *Chemistry of Materials* 2015, **27**:1855-1862.
33. Chen S, Wang L-W, Walsh A, Gong XG, Wei S-H: **Abundance of [Cu_{Zn} + Sn_{Zn}] and [2Cu_{Zn} + Sn_{Zn}] defect clusters in kesterite solar cells**. *Applied Physics Letters* 2012, **101**:223901-223904.
34. Chen S, Walsh A, Yang J-H, Gong XG, Sun L, Yang P-X, Chu J-H, Wei S-H: **Compositional dependence of structural and electronic properties of Cu2ZnSn(S,Se)4 alloys for thin film solar cells**. *Physical Review B* 2011, **83**:125201.
35. Chen SY, Yang JH, Gong XG, Walsh A, Wei SH: **Intrinsic point defects and complexes in the quaternary kesterite semiconductor Cu2ZnSnS4**. *Physical Review B* 2010, **81**:245204-245214.
36. Todorov TK, Tang J, Bag S, Gunawan O, Gokmen T, Zhu Y, Mitzi DB: **Beyond 11% Efficiency: Characteristics of State-of-the-Art Cu2ZnSn(S,Se)4 Solar Cells**. *Advanced Energy Materials* 2013, **Vol. 3**:34-38.
37. Mendis BG, Goodman MCJ, Major JD, Taylor AA, Durose K, Halliday DP: **The role of secondary phase precipitation on grain boundary electrical activity in Cu[sub 2]ZnSnS[sub 4] (CZTS) photovoltaic absorber layer material**. *Journal of Applied Physics* 2012, **112**:124508-124510.
38. Chen S, Walsh A, Gong X-G, Wei S-H: **Classification of Lattice Defects in the Kesterite Cu2ZnSnS4 and Cu2ZnSnSe4 Earth-Abundant Solar Cell Absorbers**. *Advanced Materials* 2013, **25**:1522-1539.
39. Collord AD, Hillhouse HW: **The effect of nanocrystal reaction time on Cu2ZnSn(S,Se)4 solar cells from nanocrystal inks**. *Solar Energy Materials and Solar Cells* 2015, **141**:383-390.
40. Ki W, Hillhouse HW: **Earth-abundant element photovoltaics directly from soluble precursors with high yield using a non-toxic solvent**. *Advanced Energy Materials* 2011, **1**:732-735.
41. Xin H, Katahara JK, Braly IL, Hillhouse HW: **8% Efficient Cu2ZnSn(S,Se)(4) Solar Cells from Redox Equilibrated Simple Precursors in DMSO**. *Advanced Energy Materials* 2014, **4**.
42. Chen SY, Gong XG, Walsh A, Wei SH: **Defect physics of the kesterite thin-film solar cell absorber Cu2ZnSnS4**. *Applied Physics Letters* 2010, **96**.
43. Walsh A, Chen S, Wei S-H, Gong X-G: **Kesterite Thin-Film Solar Cells: Advances in Materials Modelling of Cu_2ZnSnS_4**. *Advanced Energy Materials* 2012, **2**:400-409.
44. Wätjen JT, Engman J, Edoff M, Platzer-Björkman C: **Direct evidence of current blocking by ZnSe in $Cu_2ZnSnSe_4$ solar cells**. *Applied Physics Letters* 2012, **100**.
45. Just J, Luetzenkirchen-Hecht D, Frahm R, Schorr S, Unold T: **Determination of secondary phases in kesterite Cu2ZnSnS4 thin films by x-ray absorption near edge structure analysis**. *Applied Physics Letters* 2011, **99**.
46. Unold T, Kretzschmar S, Just J, Zander O, Schubert B, Marsen B, Schock H: **Correlation between composition and photovoltaic properties of Cu2ZnSnS4 thin film solar cells**. In *Photovoltaic Specialists Conference (PVSC), 2011 37th IEEE*; 2011:002820-002823.

47. Collord AD, Xin H, Hillhouse HW: **Combinatorial Exploration of the Effects of Intrinsic and Extrinsic Defects in Cu2ZnSn(S,Se)(4)**. *Ieee Journal of Photovoltaics* 2015, **5**:288-298.
48. Shu Q, Yang J-H, Chen S, Huang B, Xiang H, Gong X-G, Wei S-H: **$Cu_2Zn(Sn,Ge)Se_4$ and $Cu_2Zn(Sn,Si)Se_4$ alloys as photovoltaic materials: Structural and electronic properties**. *Physical Review B* 2013, **87**:115208.
49. Ford GM, Guo Q, Agrawal R, Hillhouse HW: **Earth abundant element Cu(2)Zn(Sn(1-x)Ge(x))S(4) nanocrystals for tunable band gap solar cells: 6.8% efficient device fabrication**. *Chemistry of Materials* 2011, **23**:2626-2629.
50. Lundberg O, Edoff M, Stolt L: **The effect of Ga-grading in CIGS thin film solar cells**. *Thin Solid Films* 2005, **480**:520-525.
51. Bleiwas DI: **Byproduct Mineral Commodities Used for the Production of Photovoltaic Cells: U.S. Geological Survey Circular 1365**. United States Geological Survey; 2010.
52. Gloeckler M, Sites JR: **Efficiency limitations for wide-band-gap chalcopyrite solar cells**. *Thin Solid Films* 2005, **480-481**:241-245.
53. Hanna G, Jasenek A, Rau U, Schock HW: **Influence of the Ga-content on the bulk defect densities of Cu(In,Ga)Se2**. *Thin Solid Films* 2001, **387**:71-73.
54. Li J, Wei M, Du Q, Liu W, Jiang G, Zhu C: **The band alignment at CdS/Cu2ZnSnSe4 heterojunction interface**. *Surface and Interface Analysis* 2013, **45**:682-684.
55. Haight R, Barkhouse A, Gunawan O, Shin B, Copel M, Hopstaken M, Mitzi DB: **Band alignment at the $Cu_2ZnSn(S_xSe_{1-x})_4$/CdS interface**. *Applied Physics Letters* 2011, **98**:253502-253503.
56. Halim MA, Islam MM, Xianjia L, Chong X, Sakurai T, Sakai N, Kato T, Sugimoto H, Tampo H, Shibata H, et al.: **Study of recombination process in Cu_2ZnSnS_4 thin film using two-wavelength excited photoluminescence**. In *Photovoltaic Specialist Conference (PVSC), 2014 IEEE 40th*; 2014:2334-2337.
57. Miller DW, Warren CW, Gunawan O, Gokmen T, Mitzi DB, Cohen JD: **Electronically active defects in the $Cu_2ZnSn(Se,S)_4$ alloys as revealed by transient photocapacitance spectroscopy**. *Applied Physics Letters* 2012, **101**:142106-142104.
58. Miller DW, Warren CW, Gunawan O, Gokmen T, Mitzi DB, Cohen JD: **Electronically active defects in the Cu2ZnSn(Se,S)(4) alloys as revealed by transient photocapacitance spectroscopy**. *Applied Physics Letters* 2012, **101**.
59. Urbach F: **The Long-Wavelength Edge of Photographic Sensitivity and of the Electronic Absorption of Solids**. *Physical Review* 1953, **92**:1324-1324.
60. Kane EO: **Thomas-Fermi Approach to Impure Semiconductor Band Structure**. *Physical Review* 1963, **131**:79-&.
61. Shklovskii BI, Efros AL: **Interband Absorption of Light in Strongly Doped Semiconductors**. *Soviet Physics Jetp-Ussr* 1971, **32**:733-&.
62. Fox M: *Optical Properties of Solids*. Oxford University Press; 2001.
63. Van Roosbroeck W, Shockley W: **Photon-Radiative Recombination of Electrons and Holes in Germanium**. *Physical Review* 1954, **94**:1558-1560.
64. Uhl AR, Katahara JK, Hillhouse HW: **Molecular-ink route to 13.0% efficient low-bandgap CuIn(S, Se)(2) and 14.7% efficient Cu(In, Ga)(S, Se)(2) solar cells**. *Energy & Environmental Science* 2016, **9**:130-134.